Characterization of a Re-entry Plasma Wind Tunnel Flow with Vacuum Ultraviolet to Near Infrared Spectroscopy

Tobias Hermann[a], Stefan Löhle[b], Fabian Zander[c], Hannes Fulge[d], Stefanos Fasoulas[e]
Universität Stuttgart, Institut für Raumfahrtsysteme,

Pfaffenwaldring 29, Stuttgart, Germany, D–70569

This paper presents the analysis of optical emission spectroscopic measurements from the vacuum ultraviolet (120 nm) to the near infrared (960 nm) in a high enthalpy air plasma flow corresponding to superorbital re-entry conditions. The vacuum ultraviolet measurements have been realized with a new experimental setup allowing measurements through a bore hole in the sample. Using the commonly applied optical emission spectroscopy from the side, the radiation transport along the line of sight of the vacuum ultraviolet measurements has been assessed. This allowed the determination of the local ground state densities of atomic oxygen and atomic nitrogen from a branching ratio analysis and the black body limiting correction of the vacuum ultraviolet radiation. Through the analysis of the absorption in the bore hole the spectra have been corrected resulting in the stagnation point radiative heat flux in the vacuum ultraviolet of 235 $\mathrm{kW/m^2}$.

[a] PhD student, High Enthalpy Flow Diagnostic Group, IRS, Member AIAA
[b] Research Scientist, High Enthalpy Flow Diagnostic Group, IRS, Member AIAA
[c] Research Scientist, High Enthalpy Flow Diagnostic Group, IRS, Member AIAA
[d] PhD student, High Enthalpy Flow Diagnostic Group, IRS, Member AIAA
[e] Professor, Director, IRS, Senior Member AIAA

Nomenclature

A_p = diameter of aperture, mm

A_{ul} = Einstein coefficient, s^{-1}

C = circle of confusion, μm

C_{error} = erroneous CCD chip count, counts

c = speed of light in vacuum, m/s

DoF = depth of field, mm

E = state energy, cm^{-1}

F_N = F-number

f = focal length, mm

g = state degeneracy

h = Planck constant, Js

h_{local} = local mass–specific enthalpy, MJ/kg

I = arc current, A

K = proportionality constant for air, $W/(MJ/kg\ Pa^{0.5}\ m^{1.5})$

k = Boltzmann constant, J/K

k_{cal} = calibration factor, $W/(m^2\,nm\,sr)/(counts/s)$

L_λ = spectral radiance, $W/(m^2\,nm\,sr)$

$L_{\lambda,\text{Limit}}$ = black body limit spectral radiance, $W/(m^2\,nm\,sr)$

M = magnification

$\dot{m}$ = mass flow, g/s

n = number density, m^{-3}

n_0 = ground state population density, m^{-3}

n_i = excited state population density, m^{-3}

P = electric power, kW

P_k = spectral line shape, nm^{-1}

p = pressure, hPa

$\dot{q}$ = heat flux, kW/m^2

R_{eff} = effective nose radius, mm

r = radial distance, mm

S = raw signal, counts/s

s = distance from the probe surface, mm

s_0 = distance between object and focusing element, mm

T = temperature, K

U = arc voltage, V

v = vibrational quantum number

x = axial distance from the nozzle, mm

y = horizontal distance from the nozzle, mm

z = vertical distance from the nozzle, mm

α_λ = absorption coefficient, m^{-1}

δ = full width at half maximum of line broadening, nm

ε_λ = emission coefficient, $\mathrm{W}/(\mathrm{m}^3\,\mathrm{nm}\,\mathrm{sr})$

ε = spectrally integrated emission coefficient, $\mathrm{W}/(\mathrm{m}^3\,\mathrm{sr})$

λ = wavelength, nm

σ_λ = absorption cross section, m^2

Subscripts

BB = black body

DL = deuterium lamp

exc = electronic excitation

IS = integrating sphere

l = lower state

rot = rotational

tot = total

trans = translational

u = upper state

vib = vibrational

I. Introduction

Vehicles entering the Earth's atmosphere on hyperbolic trajectories, e.g. sample return or planetary return missions feature high entry velocities. This leads to very high heat loads, which originate from the strong shock wave ahead of the vehicle [1]. The only successful concept for thermal protection at these load levels is ablation. Heat shields consisting of ablative materials withstand the high heat loads through a combination of several effects: the hot surface reduces the heat transfer at the wall and increases the re-radiation of heat; pyrolysis processes inside the material lead to an outgassing which keeps the hot plasma flow (further) away from the surface; and chemical and thermal decomposition consumes heat through oxidation, nitridation, and sublimation [2–5]. At the Institute of Space Systems (IRS) of the University of Stuttgart, plasma wind tunnels have been developed to provide high enthalpy plasma flows for fundamental thermal protection material testing [6–9]. These facilities, developed in the 1980s, have been designed to simulate the thermochemical state in the boundary layer in front of a thermal protection material.

The thermal load encountered consists of two types, convective heat flux and radiative heat flux. As the re-entry speed increases, radiative heating becomes more and more dominant [10–12]. It has previously been found that the vacuum ultraviolet (VUV) spectral region, the 100-200 nm wavelength interval, contributes a major part to the total radiative heat flux [5, 13–17]. Ablative materials interact with the flowfield which can have a significant effect on the radiative heat flux encountered by the vehicle. Both increases and decreases in radiative heating through ablation have been reported in numerical analyses [2, 18, 19]. Furthermore, the lack of experimental data results in large uncertainties in numerical calculations due to the dominant role of the VUV spectral region on the total radiative heat flux [14]. Therefore, experimental investigations of this spectral region are important to validate numerical models for the prediction of thermal loads on a re-entry vehicle. VUV experimental investigations are rather rare, which is due to the high complexity when considering VUV radiation detection. The only flight data available to date belongs to the Fire II re-entry mission where the influence of VUV radiation was assessed [20, 21]. Furthermore, VUV radiation has been investigated extensively in impulse facilities [22–26]. The first investigations of VUV radiation in a plasma wind tunnel at IRS were conducted by Röck utilizing radiometric mea-

surements which confirmed the significance of this spectral region for the overall radiative heat flux in a nitrogen plasma [27]. However, to the knowledge of the authors there is only the publication of Palumbo et al. which shows optical emission spectroscopic measurements in the VUV wavelength interval in a plasma wind tunnel [28]. Due to the steady test conditions plasma wind tunnels are suited to investigate the coupling between ablation and radiation. Therefore, these facilities need to be adapted to be able to conduct emission spectroscopic measurements of VUV radiation. However, the magnitude of VUV radiation, the accuracy of spectroscopic constants and absorption processes complicate the analysis of the measurements [29].

In order to enable investigations adressing these issues, a VUV spectroscopic setup has been installed in the plasma wind tunnel PWK1 at IRS. The setup measures the radiation entering a bore hole (diameter 2 mm) in the stagnation point of a probe (diameter 80 mm) in the spectral range from 116 to 196 nm **with a spectral resolution of 0.01 nm/px and a Voigt width of 0.07 nm (full width at half maximum)**. The probe setup is capable of operating with a water cooled copper sample or with ablative material samples. Measurements are conducted through a magnesium fluoride window which is mounted 15 mm behind the sample's surface. This paper presents how the measured spectra are calibrated to a resulting VUV spectrum at the stagnation point. In order to evaluate the measured VUV spectra, additional spectroscopic measurements are conducted with an ultraviolet to near infrared (UV-NIR) spectroscopic system viewing the plasma from the side through a window in the vessel [30].

The hardware used for the investigation was provided by the Ecole Polytechnique Federale de Lausanne (EPFL) and the Center for Hypersonics at the University of Queensland (UQ), in the frame of a joint research project supported by the European Space Agency (ESA).

As a first step the VUV radiation in front of a cooled copper sample is studied, i. e. the radiation without influence of ablative phenomena. This paper presents a detailed setup in order to provide calibrated VUV and UV-NIR optical emission spectra. These spectra are then further reduced to determine excitation temperatures and population densities of ground and metastable states of atomic oxygen and nitrogen. The final result is the VUV spectral radiance incident on the sample surface at the stagnation point which **clearly shows** the significance of VUV radiation.

II. Facility Overview

All experiments have been conducted in the plasma wind tunnel PWK1, which consists of a vessel with a 2 m diameter and 6 m length. It is connected to a vacuum pumping system consisting of a roots type pump system with four stages. The plasma generator used is the magnetoplasma-dynamic arcjet generator RD5 which allows high local mass specific enthalpy testing [31]. Electric power is provided by a current-regulated thyristor rectifier consisting of six identical units supplying 1 MW each. Samples are mounted in probes which are installed on a movable platform operated by a CNC stepping motor. The equipment inside the vessel is water-cooled with a water pressure of 16 bar to keep the temperatures of the probe and auxiliary equipment below critical material values. All experimental results presented here have been measured in a flow condition corresponding to a Hayabusa re-entry trajectory point at 78.8 km altitude with a velocity of 11.7 km/s [32]. This ground testing flow condition is set according to the concept of the local heat transfer simulation which relates a subsonic boundary layer to a hypersonic real flight condition [33]. This concept is based on the duplication of the boundary layer defined by the local mass-specific enthalpy, the stagnation point pressure and the velocity gradient at the edge of the boundary layer. Heat flux and stagnation pressure have been measured. A combined total pressure and heat flux probe with a diameter of 80 mm at an axial distance of 270 mm from the nozzle was used [34]. The local mass-specific enthalpy was calculated using the semi-empirical relation of Zoby,

$$h_{\mathrm{local}} = \frac{\dot{q}_{\mathrm{fc}}}{K} \cdot \sqrt{\frac{R_{\mathrm{eff}}}{p_{\mathrm{tot}}}}, \tag{1}$$

where $\dot{q}_{\mathrm{fc}}$ is the fully catalytic heat flux, $R_{\mathrm{eff}} = 2.3 \cdot R$ is the effective nose radius, p_{tot} is the total pressure at the stagnation point and $K = 367\,\mathrm{W/(Pa^{0.5}\ m^{1.5}\ MJ/kg)}$ is the constant for air [35]. Total pressure and heat flux have been measured during the calibration of the flow condition. Eq. (1) was derived under the assumption of a hypersonic flow in thermal equilibrium, where heat flux is measured on a fully catalytic surface. Some of these conditions are not met in the investigated subsonic flow. However, previous investigations of other subsonic flows in the same facility have shown that results obtained with this method are comparable to results of other measurement techniques [34, 36, 37]. Thus, the method is assumed to result in a reasonable estimate of the local

Table 1 Plasma wind tunnel condition parameters.

Parameter		Value
Mass flow (air)	$\dot{m}$	18.0 g/s
Ambient pressure	p_∞	16.6 hPa
Stagnation pressure	p_{tot}	24.4 hPa
Arc current	I	1220 A
Arc voltage	U	133 V
Electric power	P	163 kW
Axial distance from the nozzle	x	270 mm
Heat flux	$\dot{q}$	4100 kW/m^2
Local mass–specific enthalpy	h_{local}	68.4 MJ/kg

mass-specific enthalpy. Further measurements of this quantity are planned in future campaigns [38]. A summary of the facility parameters needed to adjust the flow condition is given in Table 1.

III. Experimental Design

In order to assess the radiative heat flux to the probe surface originating from the VUV spectral region, and thus enabling ablation-radiation coupling investigations, a VUV spectroscopic system has been installed in the plasma wind tunnel PWK1. UV-NIR spectroscopy is conducted viewing the flow field from the side to further analyze the measured VUV spectra.

A. VUV Spectroscopy

1. Overview of the setup

A schematic of the VUV spectroscopic system is shown in Fig. 1. Spectroscopic measurements require the radiation of interest to be transmitted into the spectrometer. For VUV radiation, this is particularly challenging as it is strongly absorbed by molecular oxygen which is present in the plasma flow and furthermore by water vapor in the ambient air. Therefore, an evacuated or purged light path is required to enable the transmission of the VUV radiation. In this configuration an evacuated light path is used sealed with a magnesium fluoride window. The vacuum system consists of two turbomolecular pumps, a Leybold Turbovac 150 (vacuum pump capacity 150 l/s) and a

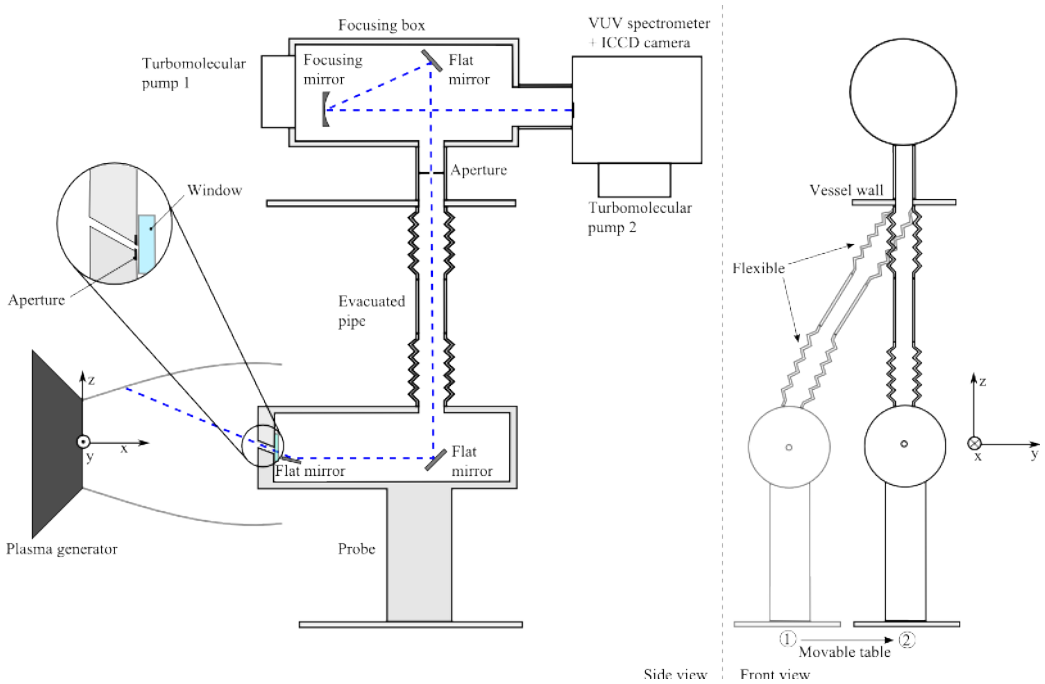

Fig. 1 Schematic setup of the VUV spectroscopic system (not to scale). Optical path shown as a dashed line.

Pfeiffer TPU 170 (vacuum pump capacity 170 l/s) and a rotary vane pump Leybold D4B (vacuum pump capacity $4\,m^3/h$)

Components of the light path in close proximity to the plasma are exposed to high heat loads. In order to protect the optical system from this heat load a high pressure water system is installed which cools the probe and the evacuated pipe.

Finally the probe front was developed such that it was interchangeable allowing different materials to be tested. This work presents the initial results using the cooled copper samples.

During the start-up procedure of the facility the probe should not be in the flow. Therefore, the spectroscopic setup has been designed to allow two probe positions. The start-up phase typically lasts about 5 min after which the steady plasma condition for testing is achieved, i. e. mass flow, ambient pressure and arc current are adjusted and monitored until the desired values are achieved and exhibit a steady behavior. During the start-up phase, the probe is positioned laterally to the plume by repositioning the movable table (position ① in Fig. 1). When the desired test condition

is achieved, the probe is repositioned into the plume center (position ② in Fig. 1). Once the probe is in the center of the vessel, the optical path is properly aligned and the radiation can be measured by the spectrometer. Typical test times are between 10 and 20 minutes.

2. Optical path

The goal of the investigation is the assessment of ablation-radiation coupling [39]. Therefore, the focus is on the measurement of the plasma emission incident on the model surface which, in the case of the VUV radiation, is achieved by looking through the sample into the boundary layer. However, looking straight into the flow means looking into the generator towards the cathode. The possible VUV radiation originating from the highly excited electric arc inside the generator is avoided by using an angled light path, the same strategy as employed by Palumbo et al. [28]. The VUV radiation enters the probe at the stagnation point through a bore hole in the sample (diameter 2 mm) at an angle of 28 ° (see Fig. 1). The light enters the evacuated volume inside the probe through a magnesium fluoride window and an aperture (diameter 1 mm), both located 20 mm behind the probe surface. The light is redirected by a series of turning mirrors out of the vessel where a concave mirror focuses the radiation onto the spectrometer slit (see Fig. 1 left). All mirrors are made of fused silica with an aluminium & magnesium fluoride coating for high VUV reflectivity [40].

The spectrometer used is an *Acton Research Corporation* VM-521-SG spectrograph with a focal length of 1 m provided by the EPFL Centre de Recherche en Physique des Plasmas. It utilizes a 15 ° angle of incidence configuration and has a concave grating with 1200 lines/mm. An Andor iStar ICCD 340T with 2048 × 512 pixel resolution (wavelength × spatial) with a Gen II intensifier is used for acquisition, provided by the Centre for Hypersonics (UQ). The actual imaged area is reduced by the intensifier in front of the CCD which has a diameter of 18 mm, corresponding to 1334 pixels on the wavelength axis. The camera is sealed with a magnesium fluoride window. The spectral range of one image is about 15 nm with a spectral resolution of 0.01 nm/px. The apparatus function was obtained by the best fit of a Voigt function to the 121.5 nm line in the spectrum of the deuterium calibration lamp and exhibits a full width at half maximum of $\delta_{\mathrm{Gauss}} = 0.06\,\mathrm{nm}$ and

$\delta_{\text{Lorentz}} = 0.02\,\text{nm}$. The intensifier was set to the maximum gain of 4000, the camera temperature was set to -30 ° C and the slit width of the spectrometer **was set to** $100\,\mu\text{m}$ for all measurements conducted.

The magnification of the focusing optics is calculated using

$$M = \frac{f}{f - s_0} \tag{2}$$

with the focal length of the concave mirror, $f = 500\,\text{mm}$, and the distance between the object and the concave mirror, $s_0 = 3211\,\text{mm}$, yielding a magnification M = 0.18 [41]. The depth of field of the setup is calculated using

$$\text{DoF} = \frac{2F_N C s_0 f^2 (s_0 - f)}{f^4 - F_N^2 C^2 s_0^2}, \tag{3}$$

where F_N is the F-number and C is the circle of confusion [42]. For the circle of confusion, the CCD pixel size of the camera is chosen ($13.5\,\mu\text{m}$). The F-number of the focusing mirror is calculated as

$$F_N = \frac{f}{A_p}, \tag{4}$$

where A_p is the diameter of the aperture stop [42]. The resulting F-number is $F_N = 167$ which yields a depth of field of DoF = 157 mm.

B. UV-NIR Spectroscopy

The UV-NIR spectroscopic setup is shown in Fig. 2. The measurement of the plasma radiation in the ultraviolet to the near infrared spectral range 300-960 nm, is conducted through a side window. Here, spatially resolved measurements have been realized. An optical system consisting of a flat turning mirror and a concave focusing mirror is used for imaging a region of 60 mm height onto the spectrometer slit [30, 34]. The optical system is focused on the center plane of the vessel, i. e. the stagnation streamline. Due to the high intensity of the plasma a combination of the Thorlabs NDUV10 and NDUV05 neutral density fused silica filters with optical densities of OD= 1 and OD= 0.5 are used for wavelength regions below 650 nm. For higher wavelengths, a NDUV40

(OD= 4) filter is used to prevent oversaturation of the CCD camera [43]. Second order spectra are excluded using a Schott OG550 bandpass glass filter (wavelengths below 550 nm are not transmitted) for wavelengths above 650 nm and a KG4 bandpass glass filter (wavelengths below 300 nm are not transmitted) for wavelengths below 650 nm [44]. All filters are mounted in front of the spectrometer entrance slit.

An Acton SpectraPro 2758 spectrograph in Czerny-Turner configuration with a slit width of 80 μm, a focal length of $f = 750$ mm, an F-number $F_N = 9.7$ and a 300 l/mm grating (blazed at 500 nm) is used. Spectra are recorded with a 1024 $\times$ 256 pixel Andor Newton DU920N-OE CCD camera. The camera is oriented such that the 1024 pixel resolution corresponds to the wavelength direction of the diffracted light, i. e. the x-component in Fig. 2, and the 256 pixel resolution corresponds to the spatial position in the plasma plume, i. e. the z-component in Fig. 2. The effective spatial resolution of the measurement volume was determined by applying the methodology of Ref. [34] and yields $\delta_{\mathrm{Gauss}} = 0.6$ mm (full width at half maximum) in the z-direction and $\delta_{\mathrm{Gauss}} = 1.6$ mm (full width at half maximum) in the x-direction. The spectral range of one acquisition is approximately 120 nm with a spectral resolution of 0.12 nm/px. **The apparatus function was determined as a best fit of a Voigt function to atomic lines originating from the spectrum of a Hg/Ar lamp and yields $\delta_{\mathrm{Gauss}} = 0.24$ nm and $\delta_{\mathrm{Lorentz}} = 0.12$ nm resulting in $\delta_{\mathrm{Voigt}} = 0.31$ nm (full width at half maximum).**

The steady state test condition allows the scanning of the whole wavelength range during one experiment. The camera temperature was set to -60 °C and the slit width of the spectrometer was set to 80 μm for all measurements conducted.

The complete spectroscopic system is mounted on a platform that can be moved parallel to the flow. This allows the measurement of the plasma at different distances to the probe surface. The measurement locations presented in this work are 2 mm, 5 mm, 10 mm, 20 mm, 35 mm and 60 mm in front of the probe surface.

In order to achieve a high spatial resolution, the optics are aligned in such a way that the upper half of the plasma plume is captured, i. e. from the stagnation streamline to the edge of the radiating plume.

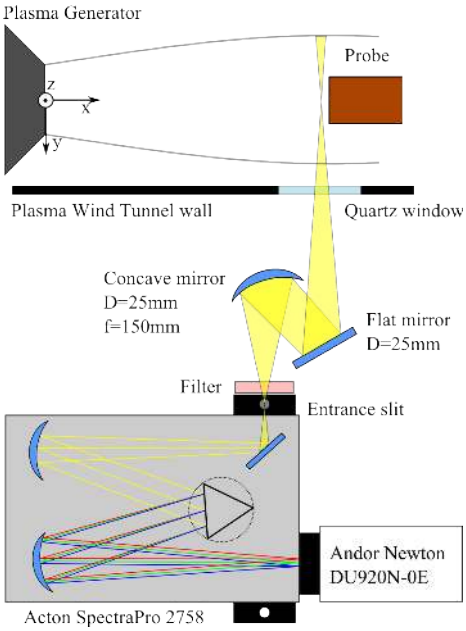

Fig. 2 UV-NIR spectroscopic setup.

The magnification of the focusing optics is calculated according to Eq. (2) with $f = 150\,\mathrm{mm}$ and $s_0 = 1520\,\mathrm{mm}$ resulting in $\mathrm{M} = 0.11$. The depth of field of the system is $\mathrm{DoF} = 89\,\mathrm{mm}$ using Eq. (3) with $F_N = 150\,\mathrm{mm}/25\,\mathrm{mm} = 6$ and $C = 80\,\mu\mathrm{m}$ which corresponds to the slit width and to approximately three pixels.

IV. Calibration

Both the VUV and the UV-NIR systems have been calibrated for absolute spectral radiance.

A. VUV Spectroscopy

The system is calibrated with a McPherson model 632 deuterium lamp which has been provided by the Centre for Hypersonics (UQ). For the calibration procedure, a calibration adapter has been designed and manufactured which allows an evacuated light path from the lamp to the window (see Fig. 3). The pressure inside the adapter is below $1 \times 10^{-4}\,\mathrm{hPa}$ to avoid additional absorption. Dowel pins position the lamp precisely at the desired angle of 28° within the depth of field of the system. With this in-situ calibration setup, the sensitivity of the complete system is accounted for.

A raw spectral image of a calibration is shown in Fig. 4. The horizontal axis corresponds to the wavelength and the vertical axis corresponds to the spatial direction which is not resolved in this

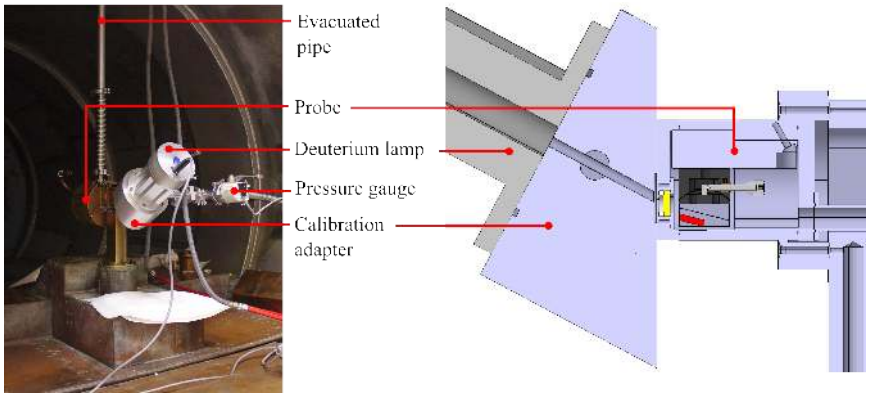

Fig. 3 A photo of the calibration setup (left) and cross sectional view of the CAD model (right).

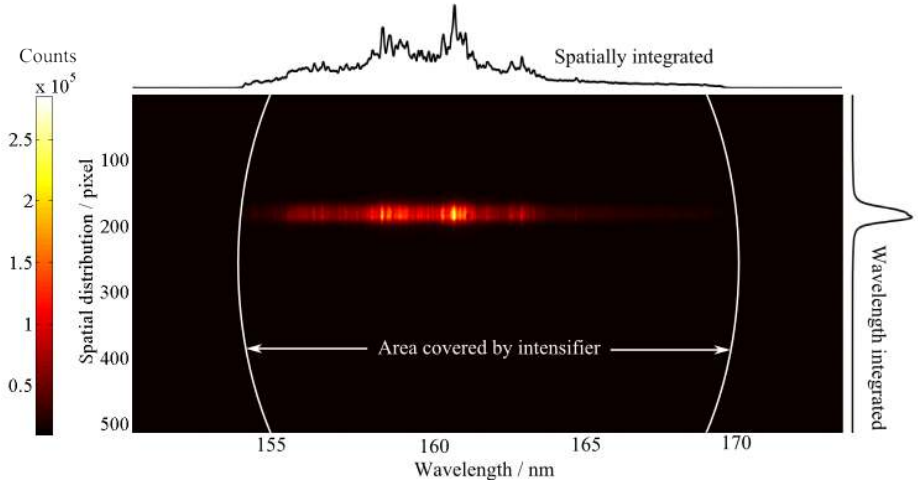

Fig. 4 Raw image of a single calibration measurement (155-170 nm).

study. In order to increase the signal to noise ratio 20 images are accumulated and summed.

A wavelength calibration is conducted based on well known molecular band heads of the calibration lamp spectrum and atomic lines of the air plasma emission [45, 46]. A polynomial fit function assigns a wavelength to each pixel. The polynomial degree differs between 1 and 2 depending on the wavelength region.

The pixel lines corresponding to the top 5 % of the wavelength integrated intensity (see the wavelength integrated value on the right in Fig. 4) are averaged and a dark frame is subtracted. The resulting data is normalized by the exposure time used to acquire the image resulting in counts per time at each wavelength. This value is then compared with the known spectral radiance of

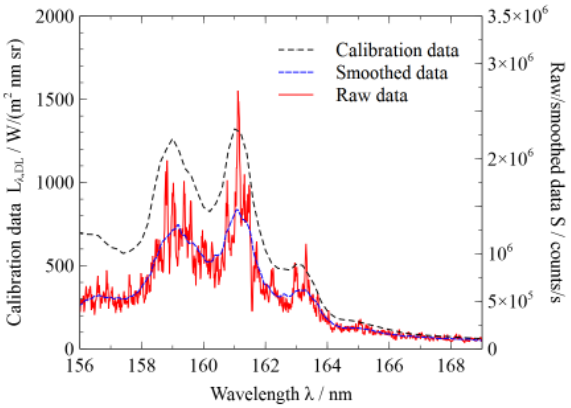

Fig. 5 Calibration data of the deuterium lamp, raw measurement data and smoothed measurement data.

the calibration lamp. As the spectrometer resolution is much greater than that provided by the calibration lamp, the measured spectrum needs to be smoothed to reproduce the spectral shape of the provided calibration data. The smoothing was done by a moving average filter with a width of 80 pixels (0.8 nm) [49]. Figure 5 shows this procedure for the wavelength interval 156-169 nm.

The calibration factor, $k_{\mathrm{cal}}(\lambda)$, is calculated by dividing the calibration lamp spectral radiance, $L_{\lambda,\mathrm{DL}}$, by the measured pixel counts per second, S,

$$k_{\mathrm{cal}}(\lambda) = \frac{L_{\lambda,\mathrm{DL}}(\lambda)}{S(\lambda)} \tag{5}$$

After this is done for every pixel, small discontinuities and noise still exist in the calibration curve. Therefore, a moving average filter with a width of 50 pixels is used on the calibration curve to reduce discontinuities and noise.

The complete spectral range investigated is divided into six single wavelength regions covering 15 nm each. The calibration curve for the entire spectral range investigated from different calibration measurements is shown Fig. 6. The wavelength ranges of the respective images are indicated as grey and white areas. The calibrated spectra are averaged in overlapping regions. The sharp drops in sensitivity (increase in k_{cal}) between these curves correspond to the edge of the intensified area of the CCD chip. The steady decrease of sensitivity towards lower wavelengths is mostly due to the window transmission.

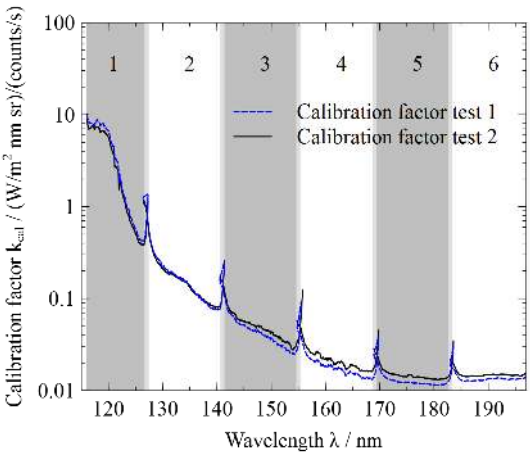

Fig. 6 Calibration factor of the complete setup in the wavelength range 116-196 nm.

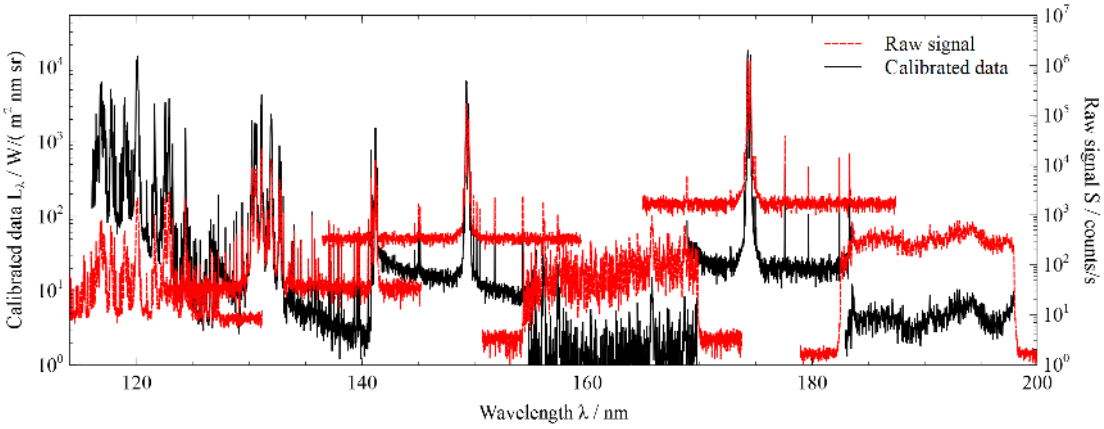

Fig. 7 Calibrated VUV spectrum and raw data in the spectral range 116-196 nm.

The calibration factor is applied to the average of the strongest 5 % of spatial pixel lines of the measurement data after a dark frame has been subtracted. The result is shown in Fig. 7 for the complete wavelength range investigated (116-196 nm) consisting of six single images (see Fig. 6).

The discontinuous offsets, e. g. at 155 nm and 170 nm, result from different recorded images. The exposure times vary from 0.01 s to 2 s depending on the spectral region. The shorter exposure times lead to a lower signal to noise ratio in regions with weak radiation which explains these discontinuous drops. The increased base level of the spectrum from 116-125 nm is most likely not a physical phenomenon. The calibration factor increases dramatically towards shorter wavelengths which leads to an amplification of noise (see Fig. 6). The constant noise level within this wavelength

region is thereby distorted by the calibration curve. The linearity of the camera has been confirmed by separate experiments for the investigated exposure times.

Due to the lateral movement of the probe after plasma ignition, small differences in the alignment of the optical setup occur from test to test. Therefore, a calibration is conducted after each test which accounts for the respective alignment of the system.

B. UV-NIR Spectroscopy

For the UV-NIR setup, a linear wavelength calibration is conducted based on atomic lines of the plasma emission. The spectroscopic system is calibrated for absolute spectral radiance using a Gigahertz-Optik BN0102 integrating sphere. The integrating sphere is positioned in the focal plane, i. e. in the center of the vacuum chamber. The lamp is moved vertically in order to calibrate each spatial pixel line of the 60 mm vertical extent of the setup and a dark frame is subtracted from the calibration image. The calibration factor $k_{\mathrm{cal}}(\lambda, y)$ is obtained by using

$$k_{\mathrm{cal}}(\lambda, y) = \frac{L_{\lambda,\mathrm{IS}}(\lambda)}{S(\lambda, y)} \tag{6}$$

with the spectral radiance of the integrating sphere $L_{\lambda,\mathrm{IS}}$ and the exposure time normalized counts of each pixel $S(\lambda, y)$. This calibration factor is then smoothed by using a **two dimensional** moving average filter of 3×3 pixels.

The complete investigated wavelength range 300-960 nm is covered by seven single acquisitions. The calibration factor of the complete investigated spectral range of the spatial pixel line 150 is plotted in Fig. 8. The discontinuity at 650 nm results from different transmissivities of the two bandpass glass filters and neutral density filters used.

Measurements of the plasma emission in this work are conducted with exposure times between 0.3 and 1 s. **After each test, a dark frame is acquired with the same settings and subtracted from the measurement**.

As the camera does not have a shutter, the CCD chip readout procedure adds an error to the measurements and it is therefore required to correct the raw measurement. The correction algorithm starts with pixel line 256 which is read out after the set exposure time has passed. The value of each

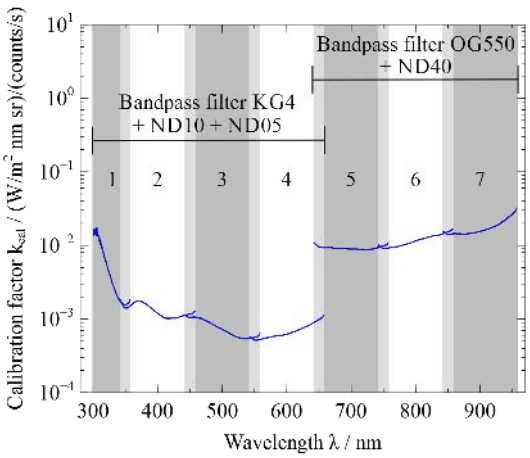

Fig. 8 Calibration factor of pixel line 150 (300-960 nm).

pixel in that line is normalized by the exposure time resulting in a raw signal strength S in counts/s. After the pixel line 256 is read out all other lines are shifted down the chip and remain in that position for the time specified by the vertical shift speed (153.8 μs). Pixel line 255, now at the bottom position of the chip, is now exposed to the radiation originally incident on pixel line 256. The amount of counts generated during that period C_{error} can be calculated using $C_{\text{error}} = S(\text{line } 256) \cdot 153.8\,\mu\text{s}$. This value is then subtracted from line 255. Line 254 has to pass through the original positions of lines 256 and 255 and is corrected for both additional exposure times. This algorithm is done accordingly for each pixel line. The raw signal and the corrected signal are presented in Fig. 9 for the atomic nitrogen multiplet at 868 nm which was acquired with an exposure time of 0.3 s. It is evident that the influence of the readout error is smallest at large pixel numbers as these lines are read out first and largest at small pixel numbers as these are read out last.

The readout-corrected images are normalized by the exposure time and multiplied with the calibration factor at each pixel. The spectrum of spatial pixel line 10 of the measurement $s = 20$ mm from the probe surface is shown in Fig. 10.

The image consists of seven single acquisitions partially overlapping each other. The exposure time of all acquisitions at this axial position is 1 s. The drop of the raw data at 650 nm is due to the different transmission of the filters used for the high and low wavelength regions respectively. However, the calibrated data matches in this overlapping region. The raw spectrum features mea-

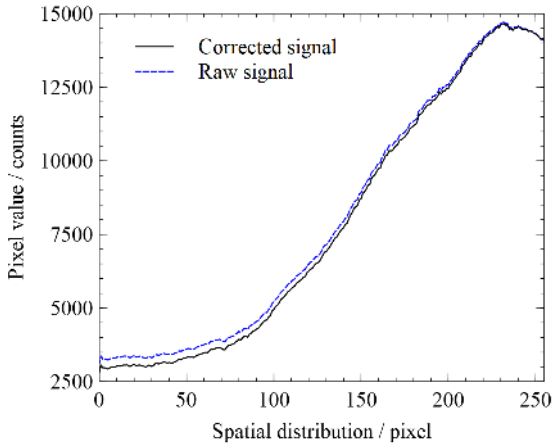

Fig. 9 Readout correction for the multiplet at 868 nm.

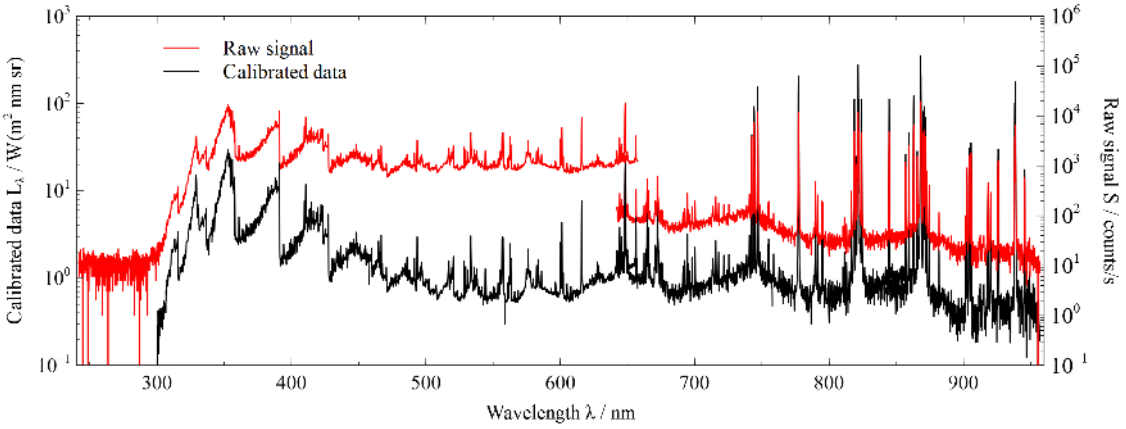

Fig. 10 Raw and calibrated data of spatial pixel line 10 (240-960 nm, $s = 20$ mm).

surement data down to 240 nm. However, the lowest calibrated wavelength of the integrating sphere is 300 nm. Thus, all measurement data below this value is omitted. The resulting spectra of all seven spectral regions are combined to a single spectrum by averaging the overlapping regions.

1. Locally resolved spectra

Assuming a rotationally symmetric plasma jet and an optically thin plasma in the measured spectral range, local emission coefficients can be calculated using Abel-transformation methods [51]. The assumption of an optically thin plasma at these wavelengths and pressures is valid [30]. To be

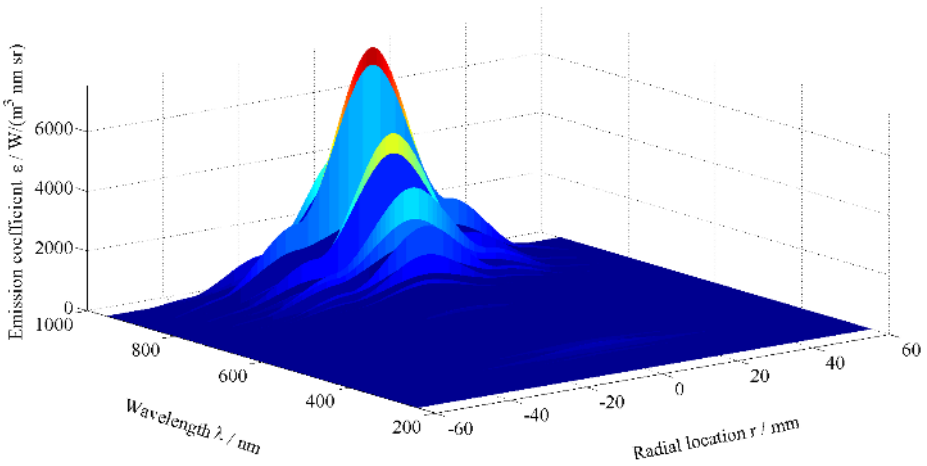

Fig. 11 Abel-transformed spectrum (300-960 nm, $s = 20$ mm).

able to use an Abel-transformation requires the measurement of the plasma jet radiation from the center line until it vanishes outside the plume. The measured data however does not completely reach zero intensity (see Fig. 9), but the parts outside the measurement volume are neglected due to their low intensity.

The algorithm used to perform the inversion is an f-interpolation type utilizing three splines. Empirical studies by Fulge et al. showed that the algorithm is accurate to within 17 % for the most common distributions expected in a plasma plume [52]. The maximum of the wavelength integrated intensity of the measured spectra is chosen as the plume center axis. Each pixel line, corresponding to a wavelength, is smoothed along the spatial direction by a moving average filter of a width of 3 pixels and is subsequently Abel-transformed. The complete Abel-transformed spectrum measured $s = 20$ mm from the probe surface is presented in Fig. 11.

V. Analysis

This section presents the analysis methodology used to derive thermodynamic properties of the flow. Local emission values in the UV-NIR spectral bandwidth are used in the following to analyze the self absorption of VUV radiation in order to correct the VUV spectra. For this purpose, excitation temperatures and number densities of highly excited states obtained from the UV-NIR spectra are used. Furthermore, the analysis allows the absorption of VUV radiation between stagnation point and window to be quantified. Thus the VUV spectrum

incident on the probe surface is reconstructed.

A. Rotational and vibrational temperature

The local emission coefficient of molecular band radiation is used to determine the rotational and vibrational temperature by matching the measured spectra to a simulation [16, 53–55] (see Fig. 12). The method utilizes the radiation database PARADE which is a line by line calculation with the input parameters being vibrational and rotational temperature and the relative number densities of the simulated species [10, 56]. Temperatures and number density ratios are varied in order to match the experimental data. Molecular band radiation of the N_2^+ first negative system ($B^2\Sigma_u^+ \rightarrow X^2\Sigma_g^+$) and N_2 second positive system ($C^3\Pi_u \rightarrow B^3\Pi_g$) is investigated [51, 57, 58]. It is assumed that the two species are Boltzmann distributed and have the same vibrational temperature $T_{\mathrm{vib,\,N_2^+}} = T_{\mathrm{vib,\,N_2}} = T_{\mathrm{vib}}$ and the same rotational temperature $T_{\mathrm{rot,\,N_2^+}} = T_{\mathrm{rot,\,N_2}} = T_{\mathrm{rot}}$ respectively. The simulated spectra are generated with a spectral resolution of 17 pm/px. The resulting dataset is convolved with a Voigt function representing the apparatus function of the spectroscopic setup. The resulting data is spline interpolated and then integrated with wavelength intervals corresponding to the spectral resolution of the spectroscopic system, i. e. 0.12 nm/px. The resulting simulated data and the measurement dataset are normalized to their respective maximum. A least squares fit algorithm minimizes the difference between the two datasets depending on the three parameters T_{rot}, T_{vib} and $n_{N_2^+}/n_{N_2}$. The relative number density is a factor to scale the relative emission of the different molecules. The emission originates from electronically excited states. Ground state densities are only available if the various collisional radiative processes, e. g. electron excitation are known [61]. Consequently, the factor $n_{N_2^+}/n_{N_2}$ is only for scaling the emission of the different species.

This procedure is conducted for every radial location at each axial location measured. **The resulting spectrum on the stagnation streamline 20 mm from the probe surface is presented in Fig. 12. The plot shows good agreement between the simulation and measurement in the wavelength range 330-470 nm.** The agreement in the wavelength range 300-330 nm is worse which is attributed to the larger uncertainty (±15 %) of the measurement in that region. **The overall error of this procedure is estimated to be approximately ±1500 K for the**

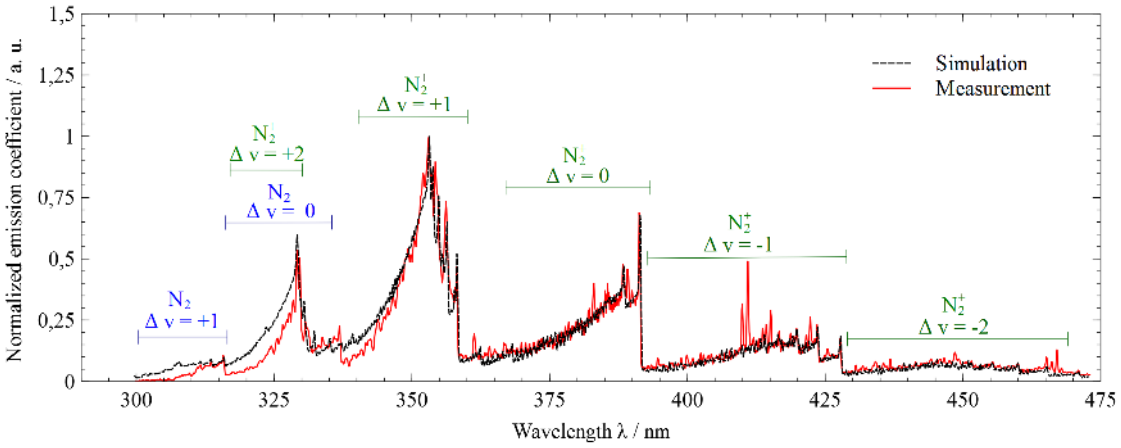

Fig. 12 Measured and simulated spectrum for the temperatures $T_{\mathrm{vib}} = 13280\,\mathbf{K}$ and $T_{\mathrm{rot}} = 11660\,\mathbf{K}$ ($s = 20\,\mathbf{mm}$, $r = 0\,\mathbf{mm}$).

presented condition.

The resulting vibrational and rotational temperature distribution is presented in Fig. 13. The figure shows that the vibrational temperature is generally higher than the rotational temperature except for regions close to the probe surface. The rotational temperature features a steeper radial gradient than the vibrational temperature which plateaus for regions $> 10\,\mathrm{mm}$ from the probe surface. In regions close to the surface, the center rotational temperature increases up to a value of 13300 K whereas in the regions further away from the probe the temperature is about 11500 K. The high temperature close to the surface shows clearly that the boundary layer is not resolved with the spatial resolution at hand. The vibrational temperature exhibits the opposite behavior. The center vibrational temperature decreases towards the probe surface to 12600 K while in the regions further away from the surface is about 13500 K. **Until the outer edge of where the measured data can be analyzed, a constant value of 10000 K is reached.** There is no information available about the temperature outside the radiating plasma flow. The distribution along the radial direction shows a mid maximum that is most likely attributed to the spline fitting in the Abel-transformation algorithm.

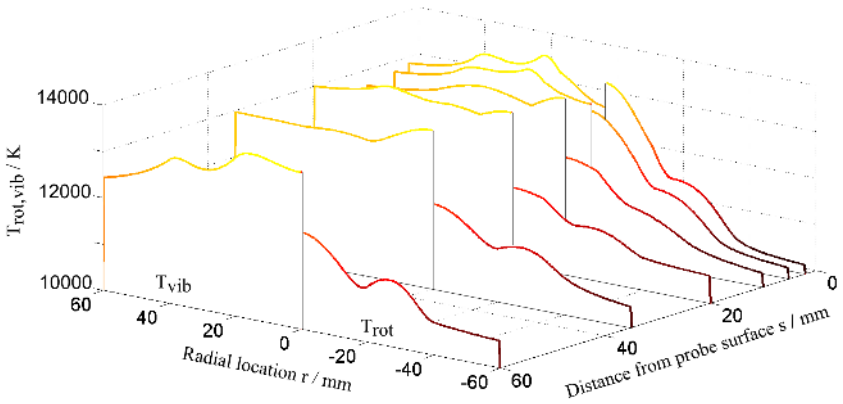

Fig. 13 Vibrational (left) and rotational (right) temperature distribution.

B. Electronic excitation temperature of atomic oxygen and nitrogen

The emission coefficients of the atomic electronic transitions are used to determine the electronic excitation temperature of the respective species using the Boltzmann plot method [30, 57, 62]. In this work atomic oxygen and atomic nitrogen are considered. The spectroscopic data is extracted from the NIST database [45]. Only multiplets are considered for the evaluation since many lines of the same multiplet overlap each other due to the limited spectral resolution of the spectroscopic system making it impossible to treat them individually. Some multiplets also overlap each other which requires them to be separated. Therefore, each line of every multiplet is simulated with a Voigt function that can be scaled to match the respective measured spectral shape [59, 60]. Each line is considered with the same Lorentz and Gauss width taking into account the apparatus function. Other broadening mechanisms are neglected as they are small compared to the apparatus function. A least squares algorithm matches the simulated line spectrum with the measured spectrum by optimizing scaling factors for each line. In cases where lines of the same multiplet are too close to separate, i. e. the distance between line centers is smaller than the spectral resolution, the resulting spectral shape is the sum of the respective lines. However, in cases where the base of measured lines overlap, i. e. the distance between line centers is bigger than the spectral resolution, the portion of each involved line is identified. The result of this fitting routine is presented in Fig. 14 for the wavelength range 855-875 nm at axial location $s = 20\,\mathrm{mm}$ from the probe surface on the stagnation line ($r = 0\,\mathrm{mm}$).

Table 2 Nitrogen multiplets used for the Boltzmann plot as listed by Ref. [45].

λ_0 / nm	A_{ul} / s^{-1}	E_u / cm^{-1}	g_u
869.4	$2.53 \cdot 10^7$	94838	20
821.4	$3.08 \cdot 10^7$	95510	12
745.4	$3.71 \cdot 10^7$	96751	4
939.8	$2.51 \cdot 10^7$	96834	10
861.9	$3.16 \cdot 10^7$	97794	6
905.2	$3.21 \cdot 10^7$	104628	6
648.7	$4.90 \cdot 10^6$	110252	28
905.0	$2.79 \cdot 10^7$	110713	14
790.7	$3.14 \cdot 10^7$	112311	6

Table 3 Oxygen multiplets used for the Boltzmann plot as listed by Ref. [45].

λ_0 / nm	A_{ul} / s^{-1}	E_u / cm^{-1}	g_u
777.6	$3.69 \cdot 10^7$	86629	15
844.9	$3.22 \cdot 10^7$	88631	9
926.6	$3.71 \cdot 10^7$	97420	25

The identified multiplets used for the evaluation of the electronic excitation temperature are summarized in Table 2 for nitrogen and in Table 3 for oxygen.

The line functions obtained for each multiplet are numerically integrated over wavelength to obtain the total emission coefficient of the respective multiplet

$$\varepsilon \left[\frac{W}{m^3 sr} \right] = \frac{n_u A_{ul} hc}{4\pi \lambda_0} \tag{7}$$

with the Einstein coefficient A_{ul}, Planck's constant h, the speed of light in vacuum c, the multiplet center wavelength λ_0 and the upper state number density n_u [51, 63]. With the measured multiplet emission coefficient, the upper state number density can be obtained. This is conducted for all investigated multiplets at every axial and radial location. The calculated upper state number

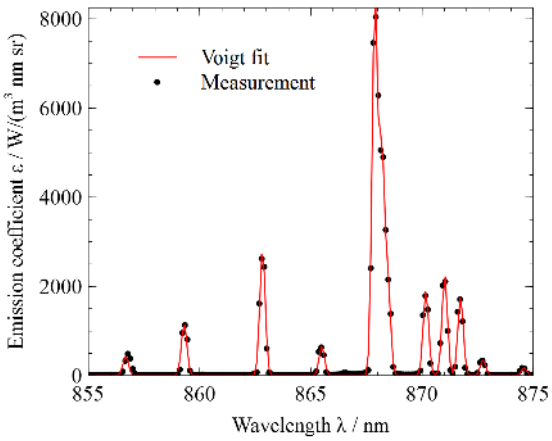

Fig. 14 Measured spectrum with Voigt fits on each spectral line ($s = 20$ mm, $r = 0$ mm).

density is weighted with the upper state degeneracy g_u and plotted against the respective upper state Energy E_u. **In a Boltzmann distribution, the different energy states are populated according to**

$$\frac{n_i}{g_i} = \frac{n_0}{g_0} \exp\left(-\frac{E_i}{kT_{\text{exc}}}\right) \tag{8}$$

with the excited and ground state number densities n_i, n_0, the respective degeneracies g_i, g_0, the excited state energy E_i, the Boltzmann constant k and the electronic excitation temperature T_{exc} [51]. The energy levels of a Boltzmann distributed atom are on a straight line when plotted logarithmically. The best linear fit in the Boltzmann plot is conducted with a least squares algorithm resulting in the electronic excitation temperature of the species.

The Boltzmann plot for the axial location $s = 20$ mm from the probe surface on the stagnation line ($r = 0$ mm) is presented in Fig. 15.

The **error bars** in Fig. 15 result from uncertainties in the spectroscopic constants, the calibration lamp data, the camera accuracy and the Abel-transformation [45, 47, 48, 50, 64, 65]. The uncertainty of the Abel-transformation is assumed to be 20 % [52]. Taking the **error bars** into account, the energy level distribution seems to be close to a Boltzmann distribution in the investigated energy range. Furthermore, the **error bars** are used to obtain an error estimate of the electronic excitation temperature by using the two least favorable possibilities to connect the measured data.

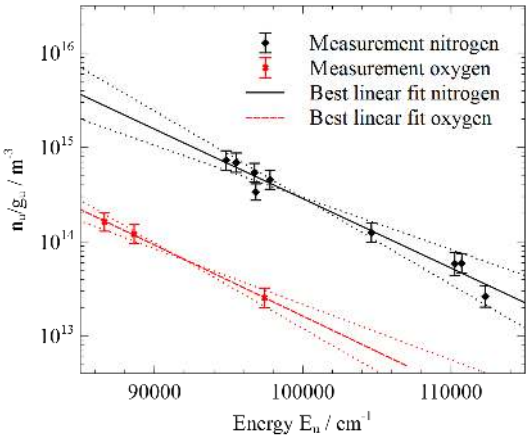

Fig. 15 Boltzmann plot for oxygen and nitrogen resulting in $T_{\mathrm{exc,\,O}}$ =8281 K (+ 2000 K - 1500 K) and $T_{\mathrm{exc,\,N}}$ =8570 K (+ 2800 K - 1700 K) (s = 20 mm, r = 0 mm).

These boundaries also indicate that an extrapolation to low lying energy levels, such as the ground state, results in large errors [21, 66, 67]. As the difference in energy of the excited states is small, the sensitivity of this method with respect to electronic excitation temperature is small, i. e. a large uncertainty in electronic excitation temperature exists [68]. The distribution of atomic energy levels throughout the flowfield behaves similarly to the distribution shown in Fig. 15. Significant deviations from a Boltzmann distribution do not occur in the investigated locations and energy range.

The calculated electronic excitation temperatures obtained from atomic oxygen and nitrogen are presented in Fig. 16. The figure shows no values for radial locations larger than 50 mm since the atomic emission is very weak at the outer edge of the plasma and thus the signal to noise ratio is too small. This also explains the behavior of the temperatures at the outer radial regions presented in Fig. 16. Oscillations of larger scale might be originating from the Abel-transformation algorithm, however, certain trends are recognizable. The center line excitation temperatures of both atoms are very similar for regions $>$10 mm from the probe surface (8200-8800 K). The center line excitation temperature of oxygen decreases towards the surface to about 6500 K while the excitation temperature of nitrogen only decreases to 7700 K. The temperature decrease of oxygen can already be seen at s = 10 mm from the surface. The temperature of nitrogen decreases slightly at s = 2 mm

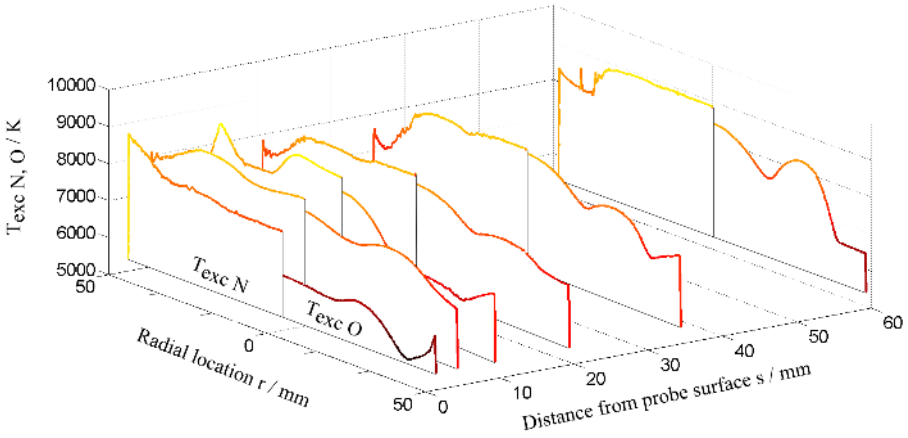

Fig. 16 Electronic excitation temperature distribution of atomic nitrogen (left) and oxygen (right).

from the surface.

C. Number density of low energy states from branching ratio analysis

The optically thick multiplets measured in the VUV spectral region have been used to determine the number density of the lower level by analyzing relative line intensities of the multiplet, i. e. the branching ratio. As the lines in a multiplet originate from a common upper state, the optically thin branching ratio only depends on spectroscopic constants and is independent of the upper state number density. However, the lines have different absorption cross sections resulting in self-absorption of different strengths for each line. The relative line intensity depends on the amount of absorption which in turn depends on the lower state number density. Thus, the measurement of the line intensity ratio is a measure for the number density of the lower level. This method has been employed for noble gases, silicon and oxygen [66, 69–72]. Furthermore, the method has been validated by a comparison to conventional absorption spectroscopy for the case of an argon plasma [73].

This method is applied here to the VUV spectrum for oxygen and nitrogen lines. Nitrogen transitions in the VUV region feature three different lower levels, the ground state and two low lying metastable states. Lower states of oxygen transitions in the VUV region also feature the ground state and two low lying metastable states [21, 45]. The multiplets considered for evaluation are listed in

Table 4 Nitrogen multiplets used for the self-absorption evaluation. [45]

λ_0 / nm	A_{ul} / s^{-1}	E_l / cm^{-1}	E_u / cm^{-1}	g_l	g_u
120.00	$4.04 \cdot 10^8$	0	83336	4	12
149.33	$3.44 \cdot 10^8$	19228	86193	10	6
124.32	$3.45 \cdot 10^8$	19228	99664	10	10
117.69	$9.77 \cdot 10^7$	19228	104196	10	6
117.09	$1.05 \cdot 10^7$	19228	104628	10	6
117.01	$1.54 \cdot 10^6$	19228	104694	10	28
116.80	$6.90 \cdot 10^6$	19228	104847	10	12
116.79	$1.04 \cdot 10^8$	19228	104851	10	14
116.58	$7.80 \cdot 10^5$	19228	105007	10	20
116.41	$3.21 \cdot 10^7$	19228	105134	10	10
174.35	$1.25 \cdot 10^8$	28839	86193	6	6
141.19	$5.39 \cdot 10^7$	28839	99664	6	10
133.59	$3.06 \cdot 10^4$	28839	103693	6	12
132.70	$9.75 \cdot 10^6$	28839	104196	6	6
131.95	$7.26 \cdot 10^7$	28839	104628	6	6
131.86	$1.46 \cdot 10^5$	28839	104675	6	28
131.63	$4.80 \cdot 10^5$	28839	104810	6	14
131.57	$2.30 \cdot 10^5$	28839	104846	6	12
131.30	$2.30 \cdot 10^5$	28839	105000	6	20
131.07	$7.73 \cdot 10^7$	28839	105134	6	10
122.87	$4.05 \cdot 10^7$	28839	110228	6	6
122.52	$4.41 \cdot 10^7$	28839	110461	6	10
119.09	$2.19 \cdot 10^7$	28839	112803	6	6
118.91	$2.48 \cdot 10^7$	28839	112938	6	10

Tables 4 and 5.

The VUV spectrum is an integral measurement of the line of sight through the bore hole. In order to apply the method to determine number densities, the radiative transport along

Table 5 Oxygen multiplets used for the self-absorption evaluation. [45]

λ_0 / nm	A_{ul} / s^{-1}	E_l / cm^{-1}	E_u / cm^{-1}	g_l	g_u
130.35	$6.12 \cdot 10^8$	78	76795	9	3
121.76	$2.06 \cdot 10^8$	33793	115918	1	3

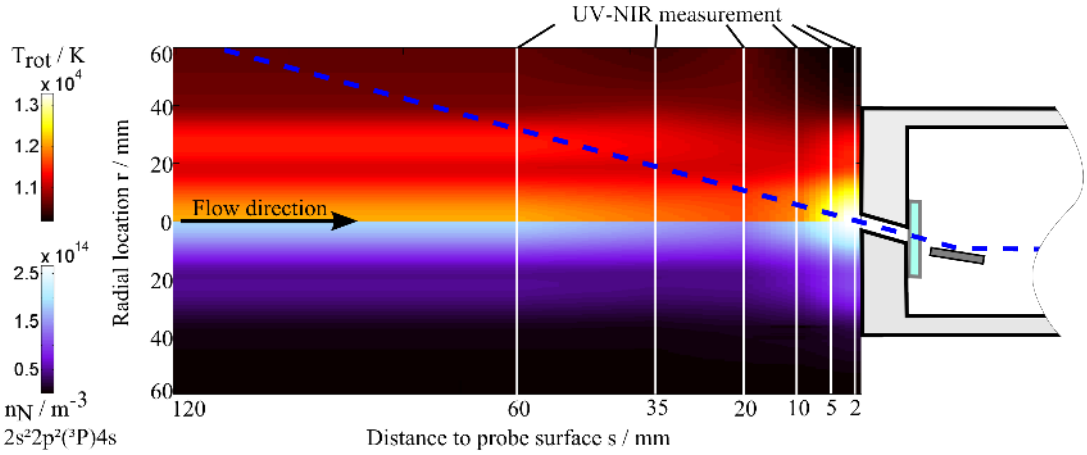

Fig. 17 Distribution of rotational temperature (upper half) and number density of the excited level $2s^2 2p^2(^3P)4s$ of atomic nitrogen (lower half).

the line of sight of the VUV spectroscopy system is required. This is realized using the UV-NIR spectroscopic data sets (see Sections V A and V B).

The electronic excitation temperature, the rotational temperature (as a measure of the translational temperature) and the population density of excited states, at every point in the flowfield are interpolated linearly between the measured values. The result for the rotational temperature and the nitrogen population density of the $2s^2 2p^2(^3P)4s$ ($E = 104196$ cm^{-1}) state is presented in Fig. 17. The figure also shows the UV-NIR measurement locations and the line of sight of the VUV spectroscopic system.

Due to the large spatial resolution in the axial direction (1.6 mm), it is not possible to resolve the boundary layer. Therefore, the 0-2 mm region was modeled by applying an assumed boundary layer distribution for atomic densities, rotational temperature and electronic excitation temperature. A parabolic distribution is used starting at 1.5 mm in front of the surface

with the values measured at 2 mm and decreasing to zero atom density and the wall temperature respectively. Additionally, it was not possible to measure at axial distances longer than 60 mm from the probe in a single experiment due to geometrical restrictions of the optical access. The flowfield properties at distances 60-120 mm from the probe surface have thus been assumed to be constant. Due to the low population density of excited states at the edge of the radiating plasma the portion of radiation contributing to the measured VUV radiance originating from this region turned out to be small. Also, a significant portion of the radiation from the plasma edge is absorbed along the optical path before it reaches the spectroscopic system.

Besides the radiating plasma, the region between stagnation point and window (23 mm length) is also considered for the radiative transport. The gas volume in this region is completely enclosed by water-cooled copper. As the aspect ratio of diameter (2 mm) to length (23 mm) is small, no significant mixing of hot plasma and cool gas is expected. A thermal analysis of the probe showed that the gas inside the hole is cooled to almost the wall temperature. Therefore, it is assumed that the temperature inside the hole is low enough to neglect atoms. The expected molecular oxygen however affects the VUV radiation measurements through absorption.

The flowfield properties along the line of sight of the VUV spectroscopic system are calculated by linear interpolation in the flowfield at 58 discrete locations. The distributions of the rotational temperature and the population densities of the atomic nitrogen states $2s^2 2p^2(^3P)3s$, $2s^2 2p^2(^3P)3p$, $2s^2 2p^2(^3P)4s$, $2s^2 2p^2(^3P)4d$ are shown in Fig. 18. The spacing between the points is smaller in the stagnation point region in order to provide a higher spatial resolution in regions of strong gradients.

The plot shows that the population density of the excited states increases towards the stagnation point. Therefore, this region is the source of the largest component of the radiation produced in the flowfield. The rotational temperature decreases from 13300 K close to the stagnation point to 10500 K at the edge of the radiating plasma while the electronic excitation temperature is almost constant at a value of approximately 8000 K except for a slight decrease at 100 mm.

The measurement volume of the VUV spectroscopy system, i. e. the line of sight, is a thin cylinder with a diameter of 1 mm (see Section III). Therefore, a one-dimensional calculation of radiative transport along the line of sight is conducted. For this, the spectral line shape in the plasma

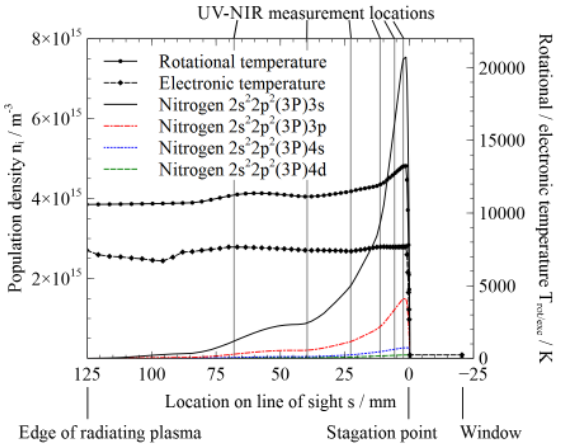

Fig. 18 Population densities of excited levels and electronic excitation temperature of atomic nitrogen and rotational temperature along the line of sight.

at every location along the line of sight is required [74]. Several line broadening mechanisms are considered. However, Doppler broadening is by far the dominating broadening mechanism and is evaluated according to Laux and assuming $T_{\mathrm{trans}} = T_{\mathrm{rot}}$ [51, 78, 79]. The line full width at half maximum (FWHM) due to natural broadening for transitions in the VUV with typical Einstein coefficients in the order of $10^8\,\mathrm{s}^{-1}$ is several orders of magnitude below Doppler broadening [51, 75]. The same is true for resonance broadening [51, 76]. Van der Waals broadening is approximated by the empirical relation given by Laux [51]. The respective FWHM is also several orders of magnitude below Doppler broadening. Stark broadening is calculated using the data provided by Johnston et al. and assuming $T_{\mathrm{e}} = T_{\mathrm{exc\,N}}$ and an equilibrium electron density of $2.9 \times 10^{21}\,\mathrm{m}^{-3}$ [80]. **The equilibrium value is calculated using the mass-specific enthalpy of 68.4 MJ/kg and the stagnation pressure of 24.4 hPa.**

The spectral shape of each line $P_k(\lambda, s)$ is evaluated at each location on the line of sight for all lines belonging to the multiplets listed in Tables 4 and 5. The radiative transport is calculated according to

$$L_\lambda(\lambda) = \int_{\text{Edge of plasma}}^{\text{Window}} \varepsilon_\lambda(\lambda, s) \cdot \exp\left(\int_s^{\text{Window}} \alpha_\lambda(\lambda, s) ds\right) ds \tag{9}$$

with the spectral emission coefficient consisting of the sum of all investigated lines

$$\varepsilon_\lambda(\lambda, s) = \sum_k \frac{n_u A_{ul} hc}{4\pi\lambda_0} P_k(\lambda, s) \tag{10}$$

and the spectral absorption coefficient consisting of the sum of all investigated lines

$$\alpha_\lambda(\lambda, s) = \sum_k \frac{g_u}{g_l} \frac{\lambda_0^4}{8\pi c} A_{ul} n_l(s) P_k(\lambda, s) + \sigma_{\lambda,\mathrm{O_2}} n_{\mathrm{O_2,hole}}(s) \tag{11}$$

with the number density of the lower, i. e. absorbing, level $n_l(s)$, the absorption cross section of molecular oxygen $\sigma_{\lambda,\,\mathrm{O_2}}$ and the respective number density $n_{\mathrm{O_2,hole}}(s)$ [66]. Cross sections for molecular oxygen are taken from Lu et al. [81]. The emission coefficient along the line of sight is calculated using the upper state population densities acquired through the UV-NIR measurements. The only unknown parameters are the distributions of the population density of the lower level of the atoms and molecular oxygen. The density of molecular oxygen is assumed to be negligible in the plasma, i. e. between the edge of the radiating plasma and the stagnation point, as oxygen is assumed to be almost completely dissociated at the temperatures at hand. However, molecular oxygen is assumed to be significant in the bore hole between stagnation point and window. Since no emission occurs in this region, the distribution of oxygen is irrelevant and only the integral value of absorption needs to be evaluated. Thus, a constant distribution is applied and Eq. (9) reduces to

$$L_\lambda(\lambda) = L_{\lambda,\,\mathrm{Plasma}}(\lambda) \cdot \exp\left(\sigma_{\lambda,\,\mathrm{O_2}} n_{\mathrm{O_2,hole}} s_{\mathrm{hole}}\right) \tag{12}$$

with the length of the bore hole s_{hole}. An estimated molecular oxygen number density is applied as a start value. The analysis of the black body limiting of lines (see next subsection) allows the calculation of the molecular oxygen number density. Thus, the analysis described in Section V C is conducted iteratively.

The distribution of the absorbing lower level n_l is modeled as the measured distribution of atomic emission of the respective species and is presented in Fig. 19.

The distribution is in qualitative agreement with atom density distributions measured in previous investigations of flows of the same plasma generator [77, 82].

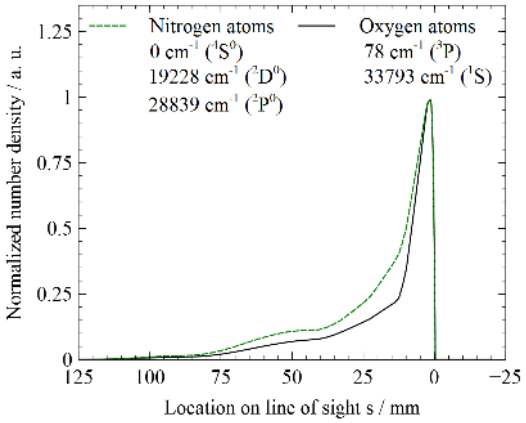

Fig. 19 Normalized distribution of number densities of absorbing levels of atomic nitrogen and atomic oxygen along the line of sight.

The radiative transport is calculated for all multiplets individually with an estimated value for the molecular oxygen number density within the bore hole. Each simulated spectrum is convoluted with the apparatus function of the spectroscopic system and normalized to the respective maximum value of the experimental measurement in the considered wavelength range. The simulation of all multiplets is compared to the measured data and a least squares fitting algorithm is applied to determine the lower level distributions $n_l(s)$, i e. the distributions in Fig. 19 are scaled. The result for all considered multiplets is shown in Fig. 20.

Figure 20 presents only excerpts of the measurement data to show the branching ratio which is only visible with a high spectral resolution. The obtained number densities are presented in a Boltzmann plot of the data from the stagnation point region ($s = 2\,\mathrm{mm}$, $r = 0\,\mathrm{mm}$) in Fig. 21, indicated as 'From VUV, branching ratio'. Additionally the high energy population densities obtained by UV-NIR spectroscopy are presented.

Figure 21 shows that the nitrogen atoms are near to a Boltzmann distribution for the measured states between $19228\,\mathrm{cm}^{-1}$ and $112311\,\mathrm{cm}^{-1}$. The oxygen atoms appear to be Boltzmann distributed for all measured states. The electronic excitation temperature obtained through a linear fit yields $T_{\mathrm{exc,N}} = 8410\,\mathrm{K}$ and $T_{\mathrm{exc,O}} = 8060\,\mathrm{K}$ respectively.

Some multiplets in the VUV spectrum are not sufficiently resolved to employ the branching ratio

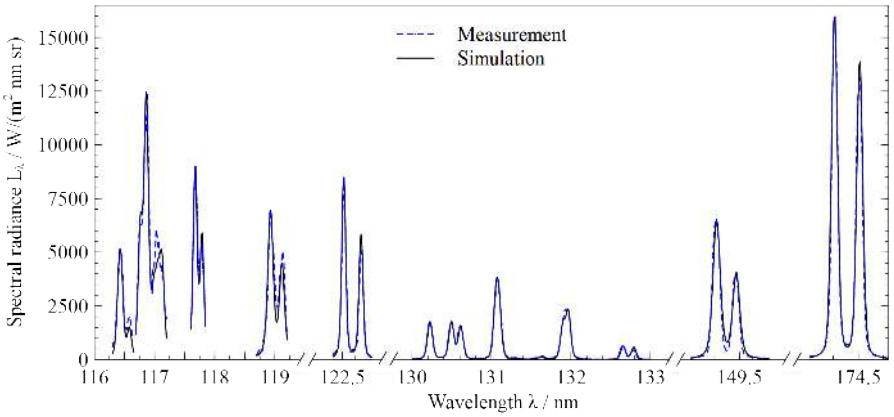

Fig. 20 Comparison between measurement data and the radiative transport simulation for stagnation point number densities $n_{\mathrm{N},19228} = 4.2 \times 10^{21}\,\mathrm{m}^{-3}$, $n_{\mathrm{N},28839} = 3.9 \times 10^{20}\,\mathrm{m}^{-3}$, $n_{\mathrm{O},78} = 6.5 \times 10^{21}\,\mathrm{m}^{-3}$.

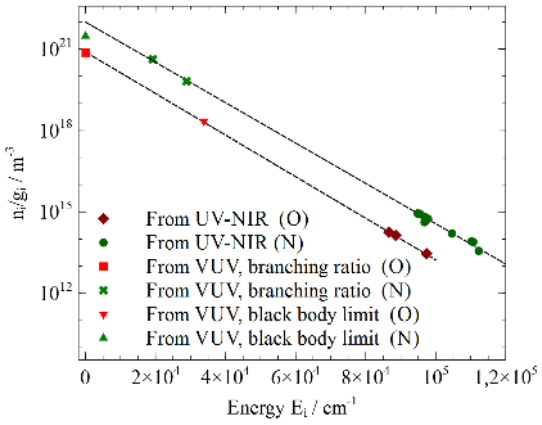

Fig. 21 Boltzmann plot for oxygen and nitrogen of the stagnation point region ($s = 2\,\mathrm{mm}$, $r = 0\,\mathrm{mm}$) with population densities acquired through UV-NIR and VUV spectroscopy.

method, e g. the nitrogen resonance triplet at 120 nm. However, with the obtained number densities from the branching ratio analysis the population density of the lower level of those transitions can be determined using the black body limit. It will be shown in the next section that many atomic lines are black body limited, i. e. their peak spectral radiance is defined by a black body temperature. Therefore, black body limiting is used to determine the black body temperature of the plasma at the stagnation point [83, 84]. Furthermore, black body limiting is used to estimate the absorption

occurring in the bore hole between window and stagnation point. This allows the calculation of the stagnation point VUV spectrum.

1. Black body limit

For optically thick emission lines, the maximum spectral radiance, i. e. the maximum of the line profile, corresponds to black body radiation according to Planck's law. The limiting criterion, i. e. how much self absorption is required that a line peak emits according to a black body is

$$\exp(-n_l \sigma_\lambda \Delta z) < 0.1 \tag{13}$$

with the absorption cross section σ_λ and a characteristic length Δz [21]. The characteristic length needed to fulfill this criterion is a fraction of a millimeter for strong lines, e. g. lines of the multiplets at 149.33 nm, 130.35 nm and 116.79 nm. Therefore, these lines are assumed to be black body limited and thus a black body temperature can be assigned to the measurement results. For the general case of a non-Boltzmann distributed atom the black body limit of a single transition is

$$L_{\lambda,\mathrm{Limit}} = \frac{2hc^2}{\lambda^5} \frac{n_u n_l^B}{n_l n_u^B} \exp\left(-\frac{hc}{\lambda k T_{\mathrm{exc}}}\right) \tag{14}$$

with the deviations from the Boltzmann distribution n_u/n_u^B and n_l^B/n_l for the upper and lower levels respectively [21].

The black body limiting applies to the actual line profile in the plasma and not to the measurement data which is a convolution of the plasma emission with the apparatus function, thus yielding a different peak value [51]. Therefore, the line profiles of each simulated multiplet are scaled in such a way that the integral of the measured multiplet matches the integral of the simulated multiplet. The spectrum obtained through this procedure is shown in Fig. 22. Figure 23 shows the multiplet at 149.33 nm at a higher spectral resolution with the respective black body limiting curve. The line shape is the result of the radiative transport along the line of sight and the dip in the center of the lines is due to self-absorption.

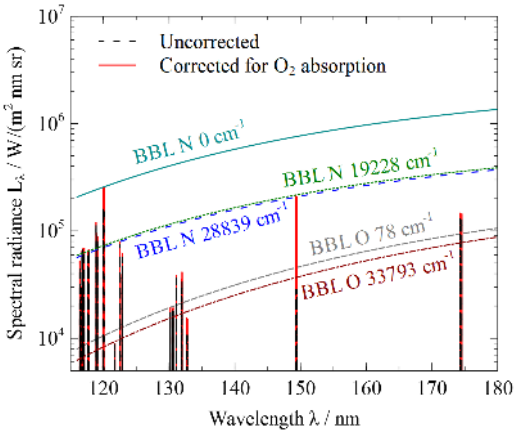

Fig. 22 Simulated spectrum at the window with correction for molecular oxygen absorption and black body limits of the respective atomic energy states.

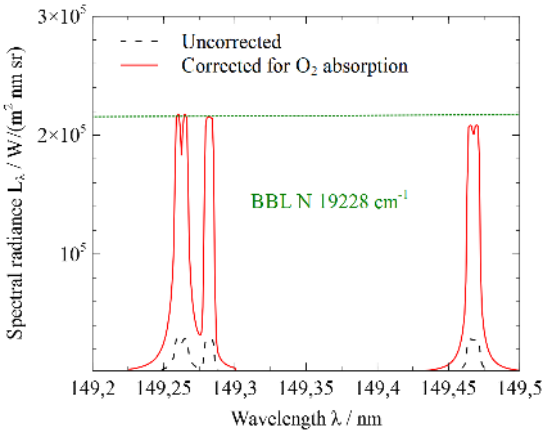

Fig. 23 Simulated spectrum at the window with correction for molecular oxygen absorption and black body limit of the 149.33 nm multiplet.

The black body limited nitrogen lines with the lower state $n_{\mathrm{N},19228}$ in the short wavelength region below 120 nm and the multiplet at 149.33 nm are used to estimate the absorption of molecular oxygen in the bore hole by utilizing their common black body limit. As these lines share the same lower state, and the UV-NIR and branching ratio data suggests that the nitrogen atom is Boltzmann distributed for the upper states of those transitions (see Fig. 21), Eq. (14) dictates that they are limited by the same Planck curve. Therefore, a black body curve is calculated which matches the limited lines in the short wavelength region yielding a temperature of $T_{\mathrm{BB,N}} = 10800\,K$ ('BBL N 19228 cm^{-1}' in Fig. 22). This curve, i. e. this temperature, applies also to the multiplet at 149.33 nm as it has the same lower state. Thus, the deviation from this curve must be due to absorption of molecular oxygen in the bore hole. With the known absorption cross section and Eq. (12), the O_2 number density is varied until the multiplet peak reaches the black body limit. The obtained number density yields $n_{\mathrm{O_2,hole}} = 6.8 \cdot 10^{22}\,\mathrm{m}^{-3}$. Assuming an air composition in the bore hole with the measured stagnation pressure (24.3 hPa) and the ideal gas law ($p = nkT$) the average temperature in the bore hole is $T_{\mathrm{hole}} = 540\,\mathrm{K}$. This temperature confirms the previous assumption of a relatively cold gas volume inside the bore hole. With the known number density of molecular oxygen, the transmission of the gas in the bore hole between stagnation point and window is evaluated. This transmission

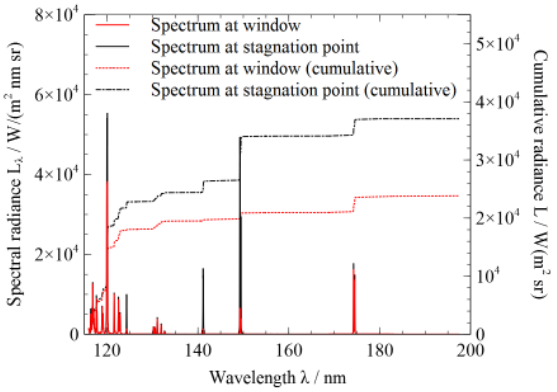

Fig. 24 Measured VUV spectrum with and without O_2 absorption correction and cumulative radiance.

is used to calculate the plasma emission correcting for the absorption in the bore hole, i. e. the radiation incident at the stagnation point. The original lines as well as the lines corrected for the molecular oxygen absorption are presented in Fig. 22.

All measured multiplets are corrected for the absorption in the bore hole by dividing each spectral line by the bore hole transmission. This correction is used to scale the measured data yielding the spectrum incident at the stagnation point (Fig. 24). This is the radiation which an ablation material sample faces in the plasma wind tunnel flow. In Fig. 24 the cumulative radiance is shown which is 1.56 times higher at the stagnation point compared to the measurement at the window. Figure 24 shows that the multiplets at 120.00 nm, 124.32 nm, 141.19 nm and 149.33 nm are affected significantly by the absorption in the bore hole while the rest of the spectrum remains almost unchanged. This is due to the spectral shape of the molecular oxygen absorption cross section [81].

The complete procedure is conducted iteratively, i. e. the obtained molecular oxygen number density is used for the radiative transport calculation of the branching ratios and the black body limits. The results presented in Figs. 20 to 24 are the final values obtained after these iterations.

Similarly, atomic oxygen is analyzed. The O_2 absorption corrected spectrum in Fig. 22 is used to obtain the black body temperature of atomic oxygen utilizing the triplet around 130.35 nm. The respective black body limit yields a temperature of $T_{\mathrm{BB,O}} = 9200\,K$ and is presented in Fig. 22. As the atomic radiation originates predominantly from the stagnation region, this temperature is

considered an average of that region.

Finally, the fact that the lines are limited by a black body curve is used to estimate relative number densities of lower levels of multiplets that are not sufficiently resolved for a branching ratio method. This is conducted for the oxygen line at 121.76 nm (^{1}S, $E = 33793\,\mathrm{cm}^{-1}$) and the nitrogen resonant triplet at 120.00 nm ($^4\mathrm{S}^0$, $E = 0\,\mathrm{cm}^{-1}$). **Due to the large transition probability of the lines and their expected number densities, the lines are expected to be black body limited. The nitrogen resonant triplet is used to obtain the number density of the ground state.** With the obtained black body temperature of nitrogen $T_{\mathrm{BB,N}}$, the peak value of the considered line and Eq. (14) the nitrogen black body limiting curve is scaled to match the line peak. The scaling factor corresponds to the deviation from the Boltzmann distribution in Eq. (14) which is used to calculate the ground state population density. The resulting number density is $n_{\mathrm{N},0} = 1.2 \cdot 10^{22}\,\mathrm{m}^{-3}$. The number density of the oxygen ^{1}S ($E = 33793\,\mathrm{cm}^{-1}$) state is calculated analogously by considering the respective values of oxygen and yields $n_{\mathrm{O},33793} = 2.2 \cdot 10^{18}\,\mathrm{m}^{-3}$. Additionally, the black body limit of the nitrogen $^2\mathrm{P}^0$ ($E = 28839\,\mathrm{cm}^{-1}$) level is calculated using Eq. (14) with the nitrogen black body temperature $T_{\mathrm{BB,N}}$ and the population density $n_{\mathrm{N},28839}$ known from the branching ratio. The respective black body limiting curves are shown in Fig. 22, while Fig. 21 presents the population densities in the Boltzmann plot. Based on a branching ratio analysis, the O_2 absorption in the bore hole and the intensity limit from black body radiation, total densities of atomic nitrogen and oxygen, their respective electronic excitation temperatures and the stagnation point spectrum were obtained.

VI. Summary

The correction for the bore hole absorption allows an estimation of the radiative heat flux incident on the stagnation point of the probe. The approximate radiative heat flux $\dot{q}_{\mathrm{rad,\,VUV}}$ from the measured VUV spectral region is

$$\dot{q}_{\mathrm{rad,\,VUV}} = 2\pi \cdot \int_{116\,\mathrm{nm}}^{196\,\mathrm{nm}} L_\lambda d\lambda = 235\,\mathrm{kW/m^2} \tag{15}$$

Table 6 Temperatures and number densities at the stagnation point region.

T_{rot} / K	T_{vib} / K	$T_{\mathrm{exc,\,N}}$ / K (UV-NIR only)	$T_{\mathrm{exc,\,O}}$ / K (UV-NIR only)	$T_{\mathrm{BBL,\,N}}$ / K	$T_{\mathrm{BBL,\,O}}$ / K
13270	12750	8410 (7700)	8060 (6490)	10800	9200

n_{N} / m^{-3} (Equilibrium calculation)	n_{O} / m^{-3} (Equilibrium calculation)
1.7×10^{22} (8.3×10^{21})	6.5×10^{21} (2.8×10^{21})

which corresponds to roughly 6 % of the total measured heat flux (see Table 1) [16]. However, the recorded spectra stem from radiation at an angle of 28 ° to the center axis. Röck showed that VUV radiation in a nitrogen plasma is highly dependent on the angle to the center axis [53]. Therefore, the relative amount of radiation of the total heat flux is probably larger than the calculated value. Population densities obtained from the self-absorption evaluation are theoretically available along the line of sight (the distribution in Fig. 19 is used). However, due to the high optical thickness of many multiplets the influence of regions further away from the stagnation point on the measured radiation is small. Therefore, only the stagnation point region is considered. The measured temperatures in this region confirm a thermal nonequilibrium and are summarized in Table 6.

Electronic excitation temperatures derived from UV-NIR measurements only yield lower temperatures compared to the temperatures obtained when the VUV measurements, i. e. lower lying states, are taken into account. Similar effects have been observed in other investigations and can be a result of strong absorption in the VUV spectral region [85, 86]. The electronic excitation temperatures obtained from all measured excited states of the two atoms match very well (within 4 %). The black body limit temperature should be identical with the electronic excitation temperature [21]. However, the difference between the two temperatures is 1140-2390 K. There are various reasons for this discrepancy. The black body temperatures are dependent on the simulated line profile. If the translational temperature of the radiating atoms differs from the measured molecular rotational

temperature, the computed line profiles may be erroneous. Furthermore, the difference between the Boltzmann plots with and without lower states has to be considered. Figure 16 shows that the temperatures decrease towards the probe surface and Table 6 shows that these temperatures (UV-NIR only) close to the probe are underestimated by 710 K and 1570 K respectively. Therefore, the temperatures far away from the probe may be larger than depicted in Fig. 16 yielding a larger black body limit. Additionally, Fig. 16 shows that the nitrogen temperature is generally higher than the oxygen temperature, a trend that is duplicated by the black body limit in the VUV spectrum. Due to the axial extent (1.6 mm full width at half maximum) of the UV-NIR measurement volume, only average values of this volume are acquired. In regions with strong gradients, i. e. the stagnation region, this spatial resolution might not suffice for the highly nonlinear nature of radiative transfer. Furthermore, the uncertainty of the measurement is largest in the short wavelength region ($\lambda < 120\,\mathrm{nm}$). However, this region is used to obtain the black body limit of the nitrogen atom. This study allows the investigation of the electronic excitation temperature using more information than the usual high energy state Boltzmann plot (see Fig. 15 with the respective error margins) and yields a temperature range of 8060-10800 K.

Although the electronic excitation temperature exhibits uncertainties, the effect on the determination of population densities is small. The branching ratio is independent of the electronic population and the spatial distribution of excited states is only a weak function of the electronic excitation temperature in the investigated flowfield. The measured states allow the calculation of atomic number densities by summing over all energy levels. The results for the stagnation point region are summarized in Table 6. These values are both approximately double of what is expected from equilibrium calculations [39]. Possibly, the thermal boundary layer increases the total number density of the gas due to a lower translational temperature close to the surface. However, due to the complex simulation, **error bars** are not easily estimated. Laity et al. approximate the uncertainty from branching ratios to be about 50 % [72].

Regarding the calculation of radiative transport, the uncertainty in the line shape has to be considered. Line wings of transitions that are strongly self-absorbed can contribute a significant amount to the total radiation incident on the probe [14]. As the electron density used in the present work

is the calculated equilibrium value, a direct measurement in future campaigns could improve the accuracy of the presented results.

This study gives first insight into the energy state distribution of the investigated atoms in the stagnation region. Oxygen appears to be completely Boltzmann distributed while nitrogen shows significant deviations for the ground state. **This ground state deviation has been predicted by numerical calculations, too [21, 67, 89]. The ground state underpopulation results in significantly larger radiation for the transitions where the ground state is the lower state [21].** The origin of this underpopulation is not yet clear. Mechanisms leading to this result could be a recombining plasma, collisional-radiative de-excitation processes or a deviation from the quasi-steady state condition [51, 67, 89–91].

Another result is that most of the VUV radiation impinging onto the probe originates from close to the surface due to the optical thickness of the lines and the high excited state population density close to the surface. The situation in flight can differ from this as a significant amount of radiation is produced in the shock [16, 92].

VII. Conclusion

For the purpose of ablation-radiation coupling investigation a VUV spectroscopy system measuring radiation in the spectral range 116-196 nm has been designed and implemented in the plasma wind tunnel PWK1 at IRS. The system measures the radiation at the stagnation point of a probe. The light is directed out of the vessel to a VUV spectrometer using a series of mirrors. Additionally, UV-NIR spectroscopic measurements in the spectral range 300-960 nm have been conducted viewing the plasma from the side. UV-NIR measurements have been conducted at five distinct axial locations and an Abel-transformation has been applied. Both spectroscopic systems have been calibrated for absolute spectral radiance.

Plasma wind tunnel tests were conducted at a local enthalpy of 68.4 MJ/kg and a stagnation pressure of 24.4 hPa. Experiments were conducted with a water-cooled copper sample as a baseline for future ablation investigations. The measured VUV spectra show strong atomic nitrogen and oxygen lines. The UV-NIR spectrum also features lines from these atomic species as well as bands from nitrogen and ionized nitrogen molecules.

The local emission coefficient of the UV-NIR measurements as well as the VUV spectral radiance have been analyzed in order to access the absorption of VUV radiation in the flow field. The VUV stagnation point spectrum has been obtained by accounting for the absorption of molecular oxygen in the probe bore hole. The measured radiative heat flux from the investigated VUV spectral range is 235 $\mathrm{kW/m^2}$ corresponding to 6 % of the total measured heat flux.

Furthermore, the VUV-NIR spectra are used to determine temperatures and number densities in the stagnation point region. Electronic excitation temperatures in the stagnation point region are in the range 8060-10800 K. The rotational and vibrational temperatures yield 13270 and 12750 K respectively. The measured number densities of atomic nitrogen and oxygen are $1.7 \times 10^{22}\,\mathrm{m^{-3}}$ and $6.5 \times 10^{21}\,\mathrm{m^{-3}}$ respectively.

The measurement of atomic metastable and ground state densities revealed that oxygen is Boltzmann distributed whereas nitrogen is Boltzmann distributed except for the ground state.

Acknowledgement

The authors gratefully acknowledge the financial support by ESA through the research grant No. 2011/ITT-6632/PL. The dedicated support of the institute's workshop is indispensable and gratefully acknowledged. The authors would like to thank the project partners for sharing their hardware and knowledge and the colleagues from the High Enthalpy Flow Diagnostics Group for the continuous and prompt help. **Additionally, the authors would like to acknowledge the input of the reviewers whose comments and suggestions increased the quality of the paper significantly.**

References

[1] Anderson, J. D., *Hypersonic and High-Temperature Gas Dynamics, 2nd Edition*, AIAA Education Series, 2nd ed., 2006.

[2] Gupta, R. N., "Aerothermodynamic Analysis of Stardust Sample Return Capsule with Coupled Radiation and Ablation," *Journal of Spacecraft and Rockets*, Vol. 37, No. 4, July 2000, pp. 507–514.

[3] Ried, R. C., Rochelle, W. C., and Milhoan, J. D., "Radiative Heating to the Apollo Command Module: Engineering Prediction and Flight Measurement," Tech. Rep. NASA-TM-X-58091, Johnson Space

Center, April 1972.

[4] Hoshizaki, H. and Lasher, L. E., "Convective and Radiative Heat Transfer to an Ablating Body," *Thermophysics Conference*, No. AIAA-67-327, AIAA, 1967.

[5] Johnston, C. O., Gnoffo, P. A., and Mazaheri, A., "Influence of Coupled Radiation and Ablation on the Aerothermodynamic Environment of Planetary Entry Vehicles," *Radiation and Gas-Surface Interaction Phenomena*, Vol. 218 of *RTO Lecture Series*, 2013.

[6] Auweter-Kurtz, M., Kurtz, H., and Laure, S., "Plasma generators for re-entry simulation," *Journal of Propulsion and Power*, Vol. 12, No. 6, November-Dezember 1996, pp. 1053–1061.

[7] Auweter-Kurtz, M. and Wegmann, T., "Overview of IRS Plasma Wind Tunnel Facilities," *RTO Educational Notes*, Vol. 8, Oct. 1999.

[8] Dabalà, P., Hilfer, G., and Auweter-Kurtz, M., "Investigation of the Oxidation Behaviour of Thermal Protection Materials Supported by Mass Spectrometry," *2nd European Symposium on Aerothermodynamics for Space Vehicles*, Nov. 1994, pp. 237–246.

[9] Laux, T., Auweter-Kurtz, M., Wegmann, T., Morino, Y., Yoshinaka, T., Park, C., and Speckmann, H. D., "Comparison of Ablation Material Tests in a Plasma Wind Tunnel and Laser Heating Facilities," *3rd European Workshop on Thermal Protection Systems*, March 1998.

[10] Liebhart, H., Herdrich, G., and Merrifield, J. A., "Advances for Radiation Modeling for Earth Re-entry in PARADE: Application to the STARDUST Atmospheric Entry," *43rd AIAA Thermophysics Conference*, AIAA, 2012.

[11] Grinstead, J. H., Jenniskens, P., Cassell, A., Albers, J., and Winter, M. W., "Airborne Observation of the Hayabusa Sample Return Capsule Re-entry," *42nd AIAA Thermophysics Conference*, AIAA, 2011.

[12] Gnoffo, P. A., "Planetary-Entry Gas Dynamics," *Annual Review of Fluid Mechanics*, Vol. 31, 1999, pp. 459–494.

[13] Na, J., Park, C., Baek, S.-W., and Muylaert, J., *Preliminary Design of Super-Orbital Earth Entry Flight Experiment Using VOLNA Launcher*, Aerospace Sciences Meetings, American Institute of Aeronautics and Astronautics, may 2008, doi:10.2514/6.2008-1129.

[14] Johnston, C. O., Mazaheri, A., Gnoffo, P. A., Kleb, B., Sutton, K., Prabhu, D., Brandis, A. M., and Bose, D., "Assessment of Radiative Heating Uncertainty for Hyperbolic Earth Entry," *42nd AIAA Thermophysics Conference*, June 2011.

[15] Park, C., "Stagnation-Point Radiation for Apollo 4," *Journal of Thermophysics and Heat Transfer*, Vol. 18, No. 3, July 2004, pp. 349–357.

[16] Laux, C. O., Winter, M., Merrifield, J. A., Smith, A., and Tran, P., "Influence of Ablation Products on the Radiation at the Surface of a Blunt Hypersonic Vehicle at 10 km/s," *41st AIAA Thermophysics Conference*, No. AIAA 2009-3925, 2009.

[17] Park, C., Abe, T., and Inatani, Y., "Research on the heatshield for MUSES-C Earth reentry," *7th AIAA/ASME Joint Thermophysics and Heat Transfer Conference*, AIAA, 1998.

[18] Park, C., "Calculation of Stagnation-Point Heating Rates Associated with Stardust Vehicle," *AIAA Journal of Spacecrafts and Rockets*, Vol. 44, No. 1, 2007.

[19] Johnston, C. O., Gnoffo, P. A., and Sutton, K., "Influence of Ablation on Radiative Heating for Earth Entry," *Journal of Spacecrafts and Rockets*, Vol. 46, 2009, pp. 481–491.

[20] Cauchon, D. L., "Radiative Heating Results from the FIRE-II Flight Experiment at a Reentry Velocity of 11.4 Kilometer per Second," Tech. Rep. TM X-1402, NASA, July 1967.

[21] Johnston, C. O. and Brandis, A. M., "Features of Afterbody Radiative Heating for Earth Entry," *11th AIAA/ASME Joint Thermophysics and Heat Transfer Conference*, Atlanta, GA, 2014.

[22] Cruden, B., Martinez, R., Grinstead, J. H., and Olejniczak, J., "Simultaneous Vacuum Ultraviolet through Near IR Absolute Radiation Measurement with Spatiotemporal Resolution in an Electric Arc Shock Tube," *41st Thermophysics Conference*, AIAA, 2009.

[23] McClenahan, J. O., "Vacuum Ultraviolet Line Radiation Measurements of a Shock-Heated Nitrogen Plasma," Tech. Rep. NASA TN D-6920, Ames Research Center, Moffet Field, California, Aug. 1972.

[24] Sheikh, U., Morgan, R., Zander, F., Eichman, T., and McIntyre, T., "Vacuum Ultraviolet Emission Spectroscopy System for Superorbital Reentries," *18th AIAA/3AF International Space Planes and Hypersonic Systems and Technologies Conference*, AIAA, 2012.

[25] Wood, A. D., Hoshizaki, H., Andrews, J. C., and Wilson, K. H., "Measurements of the Total Radiant Intensity of Air," *AIAA Journal*, Vol. 7, No. 1, Jan. 1969, pp. 130–139.

[26] Sutton, K., "Air radiation revisited," *AIAA 19th Thermophysics Conference*, June 1984.

[27] Röck, W. and Auweter-Kurtz, M., "Experimental Investigation of Huygens Entry into the Titan Atmosphere within a Plasma Wind Tunnel," June 19-22 1995.

[28] Palumbo, G., Craig, R. A., Whiting, E., and Park, C., "Measured Specific Intensity from 130 to 900nm at the Stagnation Point of a Model in an Arcjet Flow of 7.8km/s," *Journal of Quantitative Spectroscopy and Radiative Transfer*, Vol. 57, No. 2, 1997, pp. 207–236.

[29] Schreiber, P. W., Hunter, A. M., and Benedetto, K. R., "Measurement of Nitrogen Plasma Transport Properties," *AIAA Journal*, Vol. 10, No. 5, May 1972, pp. 670–674.

[30] Winter, M. W., *Emissionsspektroskopische Untersuchung der Umströmung von Probenkörpern in hochenthalpen Plasmaströmungen*, Ph.D. thesis, Institut für Raumfahrtsysteme, Stuttgart, 2007.

[31] Laure, S., *Experimentelle Simulation der Staupunktströmung wiedereintretender Raumflugkörper und deren Charakterisierung mittels mechanischer Sonden*, Dissertation, Universität Stuttgart, Institut für Raumfahrtsysteme, 1998.

[32] Löhle, S., Brandis, A., Hermann, T., and Peter, J., "Numerical Investigation of the Re-entry Flight of Hayabusa and Comparison to Flight and Ground Testing Data," *43rd AIAA Thermophysics Conference*, AIAA, LA, 2012.

[33] Kolesnikov, A. F., "Extrapolation from High Enthalpy Tests to Flight Based on the Concept of Local Heat Transfer Simulatinon," *Measurement Techniques for High Enthalpy and Plasma Flows*, No. 8B, VKI, RTO — Research and Technology Organization, Rhode–Saint–Genese, Belgium, 1999.

[34] Wernitz, R., Eichhorn, C., Herdrich, G., Löhle, S., Fasoulas, S., and Röser, H.-P., "Plasma Wind Tunnel Investigation of European Ablators in Air Using Emission Spectroscopy," *42nd AIAA Thermophysics Conference*, 2011.

[35] Zoby, E. V., "Empirical Stagnation-Point Heat-Transfer Relation in Several Gas Mixtures at High Enthalpy Levels," *NASA Technical Note*, , No. TN D-4799, 1968.

[36] Stöckle, T., *Untersuchung der Oberflächenkatalyzität metallischer und keramischer Werkstoffe in Hochenthalpieströmungen*, Dissertation, Universität Stuttgart, Institut für Raumfahrsysteme, 2000.

[37] Eswein, N., Herdrich, G., Fasoulas, S., and Röser, H.-P., "Investigation of Graphite Ablation at IRS," *42nd Thermophysics Conference*, AIAA, 2011.

[38] Löhle, S., Steinbeck, A. and Fasoulas, S., "Local Mass-Specific Enthalpy Measurements with a New Mass Injection Probe," *Jornal of Thermophysics and Heat Transfer*, 2015, in press.

[39] Löhle, S., Hermann, T., Zander, F., Fulge, H., and Marynowski, T., "Ablation Radiation Coupling Investigation in Earth Re-entry Using Plasma Wind Tunnel Experiments," *30th Aerodynamic Measurement Technology and Ground Testing Conference*, AIAA, 2014.

[40] eSource Optics, *http://www.esourceoptics.com/vuvmirrors.html*, Aug. 2014.

[41] Träger, F., *Springer Handbook of Lasers and Optics*, Springer, 2007.

[42] Pedrotti, F., Pedrotti, M., and Pedrotti, S., *Introduction to Optics*, Addison-Wesley, 3rd ed., 2006.

[43] Thorlabs GmbH, *http://www.thorlabs.de*, 2014.

[44] SCHOTT AG, *http://www.schott.com*, 2014.

[45] National Institute of Standards and Technology, *http://physics.nist.gov/PhysRefData/ASD*, 2014.

[46] Becker, K. and McConkey, J. W., "Absolute cross sections for D2 Lyman and Werner band excitation by controlled electron impact," *Canadian Journal of Physics*, Vol. 62, 1984, pp. 1–9.

[47] Thorne, A., Litzén, U., and Johansson, S., *Spectrophysics: Principles and Applications*, Springer, 1999.

[48] "CCD Image Sensor Noise Sources," Tech. Rep. MTD/PS-0233, Eastman Kodak Company, Rochester, New York, Aug. 2001.

[49] Sheikh, U., *Re-Entry Radiation Aerothermodynamics in the Vacuum Ultraviolet*, Ph.D. thesis, University of Queensland, 2014.

[50] Howell, S. B., *Handbook of CCD Astronomy*, Cambridge University Press, 2000.

[51] Laux, C. O., *Optical Diagnostics and Radiative Emission of Air Plasmas*, Ph.D. thesis, Stanford University, 1993.

[52] Fulge, H., Knapp, A., Eichhorn, C., Wernitz, R., Loehle, S., Fasoulas, S., and Herdrich, G., "Improved Abel Inversion Method for Analysis of Spectral and Photo-Optical Data of Magnetic Influenced Plasma Flows," *42nd AIAA Plasmadynamics and Lasers Conference*, 2011.

[53] Röck, W., *Simulation des Eintritts einer Sonde in die Atmosphäre des Saturnmondes Titan in einem Plasmawindkanal*, Ph.D. thesis, Institut für Raumfahrtsysteme, Universität Stuttgart, Germany, 1999.

[54] Löhle, S., Wernitz, R., Herdrich, G., Fertig, M., Röser, H.-P., and Ritter, H., "Airborne Re-entry Observation Experiment SLIT: UV Spectroscopy during Stardust and ATV1 Re-entry," *CEAS Space Journal*, Vol. 1, No. 1, 2010.

[55] Wernitz, R., Eichhorn, C., Marynowski, T., and Herdrich, G., "Plasma Wind Tunnel Investigation of European Ablators in Nitrogen/Methane Using Emission Spectroscopy," *Hindawi International Journal of Spectroscopy*, Vol. 2013, 2013.

[56] Smith, A. J., Wood, A., Dubois, J., Fertig, M., Liebhart, H., and Pfeiffer, B., *Plasma Radiation Database PARADE V2.3*, 2009.

[57] Fletcher, D. G., "Nonintrusive Diagnostic Strategies for Arcjet Stream Chracterization," *Measurement Techniques for High Enthalpy and Plasma Flows*, VKI, RTO — Research and Technology Organization, Rhode–Saint–Genese, Belgium, 1999.

[58] Löhle, S., Lein, S., Eichhorn, C., Herdrich, G., and Winter, M., "Spectroscopic investigation of an inductively heated CO2 plasma for Mars entry simulation," *Journal of Technical Physics*, Vol. 50, No. 3, 2009, pp. 151–164.

[59] Liu, Y., Lin, J., Huang, G., Guo, Y., and Duan, C., "Simple empirical analytical approximation to the voigt profile," *Journal of the Optical Society of America B*, Vol. 18, No. 5, 2001, pp. 666–672.

[60] Olivero, J. J. and Longbothum, R. L., "Empirical Fits to the Voigt Line Width: A Brief Review," *Journal of Quantitative Spectroscopy and Radiative Transfer*, Vol. 17, 1977, pp. 233–236.

[61] Popa, S. D., "Influence of pressure on spectral intensities in a flowing nitrogen glow discharge," *Journal of Physics D: Applied Physics*, Vol. 29, No. 2, 1996, pp. 416–418.

[62] van der Sijde, B. and van der Mullen, J. A. M., "Temperature Determination in non-LTE Plasmas," *Journal of Quantitative Spectroscopy and Radiative Tranfer*, Vol. 44, No. 1, 1990, pp. 39–46.

[63] Hilborn, R. C., "Einstein Coefficients, Cross Sections, f Values, Dipole Moments, and all that," *American Journal of Physics*, Vol. 50, No. 11, 1981, pp. 982–986.

[64] Taylor, J. R., *An Introduction to Error Analysis*, University Science Books, Sausalito, California, second edition ed., 1982.

[65] Mortara, L. and Fowler, A., "Evaluations Of Charge-Coupled Device (CCD) Performance For Astronomical Use," *Solid-State Imagers for Astronomy*, Vol. 290, No. 28, 1981.

[66] Stirn, R., *Emissionsspektroskopische Untersuchungen der Wechselwirkung eines Freistrahls mit Hitzeschutzmaterialien*, Ph.D. thesis, Institut für Plasmaforschung der Universität Stuttgart, Dec. 2005.

[67] Johnston, C. O., Hollis, B. R., and Sutton, K., "Non-Boltzmann Modeling for Air Shock-Layer Radiation at Lunar-Return Conditions," Tech. rep., Langley Research Center, NASA Langley Research Center, Hampton, VA, 23681, 2008.

[68] Fletcher, D. G., "Arcjet Flow Properties Determined from Laser-Induced Fluorescence of Atomic Nitrogen," *Appl. Opt.*, Vol. 38, No. 9, Mar 1999, pp. 1850–1858.

[69] Schulze, M., Yanguas-Gil, A., von Keudell, A., and Awakowicz, P., "A robust method to measure metastable and resonant state densities from emission spectra in argon and argon-diluted low pressure plasmas," *Journal of Applied Physics*, Vol. 41, Feb. 2008.

[70] Jentschke, H., Schumacher, U., and Hirsch, K., "Studies of Silicon Erosion in Plasma-Target-Interaction from Optical Emission and Absorption Spectroscopy," *Contributions to Plasma Physics*, Vol. 38, No. 4, 1998, pp. 501–512.

[71] Laity, G., Fierro, A., Dickens, J., Neuber, A., and Frank, K., "Simultaneous measurement of nitrogen and hydrogen dissociation from vacuum ultraviolet self-absorption spectroscopy in a developing low temperature plasma at atmospheric pressure," *Applied Physics Letters*, Vol. 102, No. 184104, May 2013.

[72] Laity, G., Fierro, A., Dickens, J., Frank, K., and Neuber, A., "A passive measurement of dissociated atom densities in atmospheric pressure air discharge plasmas using vacuum ultraviolet self-absorption spectroscopy," *Journal of Applied Physics*, Vol. 115, No. 123302, March 2014.

[73] Boffard, J. B., Jung, R. O., Lin, C. C., and Wendt, A. E., "Measurement of metastable and resonance level densities in rare-gas plasmas by optical emission spectroscopy," *Plasma Sources Science and Technology*, Vol. 18, June 2009, pp. 1–11.

[74] Habib, A. A. M., "Self-absorption quantification in the case of SF6-N2 thermal plasma mixture," *Journal of Quantitative Spectroscopy and Radiative Transfer*, Vol. 113, 2012, pp. 2146–2154.

[75] Laity, G., *A Radiative Model for Determining Plasma Dissociation Using Vacuum Ultraviolet Self-Absorption Spectroscopy*, Ph.D. thesis, Texas Tech University, May 2013.

[76] Griem, H. R., *Plasma Spectroscopy*, McGraw-Hill Book Company, 1964.

[77] Fasoulas, S., Sleziona, P. C., Auweter-Kurtz, M., Habiger, H., Laure, S., and Schönemann, A., "Characterization of a Nitrogen Flow within a Plasma Wind Tunnel," *AIAA Journal of Thermophysics and Heat Transfer*, Vol. 9, No. 3, 1995, pp. 422–431.

[78] Park, C., "Assessment of two-temperature kinetic model for ionizing air," *Journal of Thermophysics and Heat Transfer*, Vol. 3, July 1989, pp. 233–244.

[79] Shimada, M., Tynan, G. R., and Cattolica, R., "Rotational and translational temperature equilibrium in an inductively coupled plasma," *Journal of Vacuum Science and Technology A*, Vol. 24, No. 1878, 2006.

[80] Johnston, C. O., Hollis, B. R., and Sutton, K., "Spectrum Modeling for Air Shock-Layer Radiation at Lunar-Return Conditions," *Journal of Spacecraft and Rockets*, Vol. 45, No. 5, 2008.

[81] Lu, C. H., Chen, K. K., Chen, H. F., Cheng, B. M., and Ogilvie, J. F., "Absorption cross section of molecular oxygen in the transition e3u-v=0 - x3g -v =0 at 38 K," *Astronomy and Astrophysics*, Vol. 520, No. A19, 2010, pp. 1–4.

[82] Fasoulas, S., *Experimentelle und theoretische Charakterisierung einer hochenthalpen Stickstoffströmung zur Wiedereintrittssimulation*, Ph.D. thesis, Institut für Raumfahrtsysteme, Universität Stuttgart, Germany, 1995.

[83] Brandis, A. M., Johnston, C. O., Cruden, B., Prabhu, D., Wray, A. A., Liu, Y., Schwenke, D. W., and Bose, D., "Validation of CO4th positive radiation for Mars entry," *Journal of Quantitative Spectroscopy Radiative Transfer*, Vol. 121, 2013, pp. 91–104.

[84] Sheikh, U., Morgan, R., and McIntyre, T., "Self-absorption of vacuum ultraviolet radiation in super-orbital flows." *5th International Workshop on Radiation of High Temperature Gases in Atmospheric Entry*, 2012.

[85] Park, C., *Nonequilibrium Hypersonic Aerothermodynamics*, John Wiley & Sons, 1990.

[86] Winter, M. W., Auweter-Kurtz, M., and Park, C., "Determination of temperatures and particle densities in a subsonic high enthalpy plasma flow from emission spectroscopic measurements," *32nd AIAA Plasmadynamics and Lasers Conference*, June 2001.

[87] Ivkovic, M., Jovicevic, S., and Konjevic, N., "Low electron density diagnostics: development of optical emission spectroscopic techniques and some applications to microwave induced plasmas," *Spectrochimica Acta Part B*, Vol. 59, No. 5, May 2004, pp. 591–605.

[88] Preston, R. C., "Spectroscopic studies of the Stark-broadened wings of Lyman-α," *Journal of Physics B: Atomic, Molecular and Optical Physics*, Vol. 10, No. 3, 1977, pp. 523–540.

[89] Park, C., "Calculation of Nonequilibrium Radiation in AOTV Flight Regimes," *AIAA 22nd Aerospace Sciences Meeting*, Jan. 1984.

[90] Kano, K., Suzuki, M., and Akatsuka, H., "Spectroscopic measurement of electron temperature and density in argon plasmas based on collisional-radiative model," *Plasma Sources Sci. Technol.*, Vol. 9, No. 3, 2000.

[91] Fierro, A., Laity, G., and Neuber, A., "Optical emission spectroscopy study in the VUV-VIS regimes of a developing low-temperature plasma in nitrogen gas," *Journal of Physics D: Applied Physics*, Vol. 45, No. 49, Nov. 2012.

[92] Allen, R. A., Rose, P. H., and Camm, J. C., "Nonequilibrium and Equilibrium Radiation at Super-Satellite Reentry Velocities," Tech. Rep. 156, AVCO-Everett Research Laboratory, Everett, Mass., Sept. 1962.